ChemCatChem

Research Article
doi.org/10.1002/cctc.202500931

Chemistry Europe
European Chemical Societies Publishing

www.chemcatchem.org

Metal Hydroxide Organic Frameworks (MHOFs) for Oxygen Evolution by Intercalation of Dicarboxylate Linkers Into β-Ni(OH)$_2$: Impact of Host Crystallinity

Alessio Nicolini,*[a] Martina Campi,[a, b] Valeria Iacomini,[a, b] Andrea Cornia,[a] Lara Gigli,[c] Adele Mucci,[a, g] Ilargi Napal Azcona,[d, e] Silvia Nappini,[d] Elena Magnano,[d] Simone Pollastri,[b, c] Roberto Biagi,[b, f, g] Marco Borsari,[a] and Francesco Tassinari*[a, g]

Ni and Ni/Fe metal hydroxide organic frameworks (MHOFs) based on aromatic dicarboxylates are attracting great interest as emerging noble metal-free catalysts for the oxygen evolution reaction (OER), during H_2 production by water splitting. They show good chemical and electrochemical stability during OER, some of them exhibiting similar catalytic activity compared to state-of-the-art catalysts (e.g., IrO_2) when isolated as nanosheets. These MHOFs are actually precatalysts and reconstruct into the active NiOOH-like phases after leaching of the organic linker under electrocatalytic alkaline conditions. Employing β-Ni(OH)$_2$ (herein indicated as NiOH-*x*) with different crystallinity (*x* = 1-low, 2-intermediate, and 3-high), we synthesized "bulk" forms of Ni$_2$(OH)$_2$(L) MHOFs (NiL-*x*) based on benzene-1,4-dicarboxylate (L = BDC^{2-}) and azobenzene-4,4′-dicarboxylate (L = AZO^{2-}) ligands. We systematically obtained highly crystalline NiBDC-*x* and NiAZO-*x* samples, regardless of NiOH-*x* crystallinity. Therefore, the intercalation of L^{2-} effectively removes stacking faults disorder even from low crystalline NiOH-1, especially for BDC^{2-}, while it is less efficient for AZO^{2-}. The OER-activities were evaluated after establishing an activation procedure combining cyclic voltammetry with diffuse-reflectance UV–vis–NIR. NiAZO-x samples resulted the most stable and efficient catalysts, NiAZO-1 being the best among them although containing ~50% in weight of residual NiOH-1, which converts superficially into highly efficient NiAZO-phase during synthesis, while retaining its high-conductivity in the inorganic bulk.

1. Introduction

The energetic efficiency of *green* hydrogen (H_2) production through electrochemical water splitting (EWS)[1] is mainly limited by the oxygen evolution reaction (OER), which possesses a sluggish kinetics that involves a multi-step four-electron transfer.[1–3] In recent years, oxides and hydroxides of 3d metals (especially Ni, Co, and Fe)[2] displayed high catalytic efficiency in alkaline media,[4–7] proving to be a feasible alternative to state-of-the art catalysts based on precious elements such as iridium (Ir) and ruthenium (Ru). In addition, metal-organic frameworks (MOFs) and metal hydroxide-organic frameworks (MHOFs) based on first row transition metals were found particularly attractive for EWS,[8–11] since their porous structures and large surface areas facilitate the diffusion of substrates and products, enhancing the overall yield of the catalytic process. The main limitation to the application of MOFs and MHOFs in EWS is their instability in aqueous solutions, especially under electrocatalytic conditions, which may even lead to a full structural collapse.[12,13]

Recently, Román–Leshkov and Shao–Horn reported a series of MHOFs[7] with general formula Ni$_2$(OH)$_2$(L), derived from four aromatic dicarboxylic acids (H_2L) of increasing length,

[a] A. Nicolini, M. Campi, V. Iacomini, A. Cornia, A. Mucci, M. Borsari, F. Tassinari
Dipartimento di Scienze Chimiche e Geologiche e UdR INSTM, Università degli Studi di Modena e Reggio Emilia, via G. Campi 103, Modena 41125, Italy
E-mail: alessio.nicolini@unimore.it
francesco.tassinari@unimore.it

[b] M. Campi, V. Iacomini, S. Pollastri, R. Biagi
Dipartimento di Scienze Fisiche, Informatiche e Matematiche, Università degli Studi di Modena e Reggio Emilia, via G. Campi 213/A, Modena 41125, Italy

[c] L. Gigli, S. Pollastri
Elettra-Sincrotrone Trieste S.C.p.A., Trieste 34149, Italy

[d] I. N. Azcona, S. Nappini, E. Magnano
CNR – Istituto Officina dei Materiali (IOM), S.S. 14 km 163.5, Trieste 34149, Italy

[e] I. N. Azcona
Dipartimento di Fisica, Università degli Studi di Trieste, P.le Europa 1, Trieste 34127, Italy

[f] R. Biagi
Istituto Nanoscienze (NANO-S3), Consiglio Nazionale delle Ricerche (CNR), via G. Campi 213/A, Modena 41125, Italy

[g] A. Mucci, R. Biagi, F. Tassinari
Centro H2-MORE, Università degli Studi di Modena e Reggio Emilia, Modena 41125, Italy

Alessio Nicolini and Martina Campi contributed equally to the work.

Supporting information for this article is available on the WWW under https://doi.org/10.1002/cctc.202500931

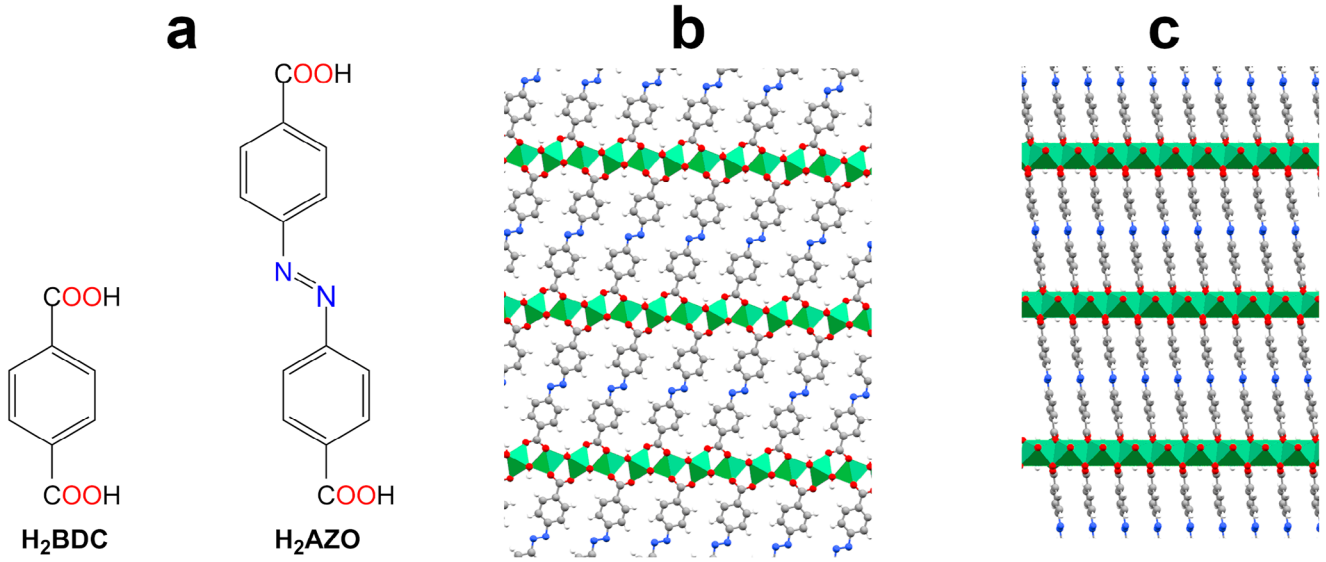

Figure 1. a) Structure of the H_2BDC and H_2AZO organic linkers. b) Front view and c) side view of the structure of NiAZO MHOF.[7] Color code: Ni = green (plotted as coordination polyhedra), O = red, N = blue, C = gray, and H = white.

from benzene-1,4-dicarboxylic acid (H_2BDC) to azobenzene-4,4′-dicarboxylic acid (H_2AZO), whose structures are reported in Figure 1. These MHOFs exhibit similar catalytic activity for OER in alkaline media compared to state-of-the-art catalysts such as IrO_2. Notably, it was recently reported that their catalytic properties are tunable by chemical modification to produce multi-metallic high-entropy MHOFs, such as $Mn_{0.4}Ni_{0.4}Co_{0.4}Cu_{0.4}Zn_{0.4}(OH)_2$(BDC),[14] whose current density at ~1.64 V versus reversible hydrogen electrode (RHE) reaches 100 mA cm^{-2}. These families of MHOFs show good stability in basic electrolyte (0.1 M aqueous KOH), due to efficient interligand π–π stacking interactions, which limit the leaching of the organic ligand from the MHOFs to the KOH solution.[7,14] However, chemical stability in alkaline environment does not necessarily reflect into stability during electrocatalysis, since the applied potential and its duration may have a significant impact on the catalytic response.[13] In addition, changes in the oxidation state of the metal centers often occur, with consequences on their coordination geometry, hardness character, etc. Therefore, Román–Leshkov and Shao–Horn subsequently decided to investigate also the long-term electrochemical stability of $Ni_2(OH)_2$(BDC) (NiBDC) and $Ni_2(OH)_2$(AZO) (NiAZO) as a function of potential and cycle number.[15] These authors found that the number of active catalytic sites and the OER activity increased with the number of cycles. They concluded that the studied MHOFs are actually precatalysts which undergo leaching of the organic ligands into the electrolyte and reconstruct into oxyhydroxide-like phases (NiOOH) that represent the real active catalysts, as also reported by Fisher et al. for NiBDC and other nickel(II)-based MHOFs with dicarboxylate linkers.[16] The leaching process is spontaneous but also enhanced by the Ni^{2+}/Ni^{3+} oxidation, leading to the complete transformation of NiBDC into NiOOH-like phase. On the other hand, due to its higher chemical stability, NiAZO reconstructs into NiOOH only superficially.[15] The differences in the catalytic activities of the activated MHOFs depend on the nature of the NiOOH phases. In particular, it has been reported that a key point is the ratio between β-$Ni(OH)_2$ and α-$Ni(OH)_2$ phases,[16] which are then oxidized during catalysis into β-NiOOH and γ-NiOOH, respectively, following Bode scheme.[17] These transformations are strongly influenced by the choice of the organic linker, which has an enduring impact on the catalytic activity of the MHOFs even after a complete transformation into NiOOH phases.

NiBDC and NiAZO can be synthesized in heterogeneous solvothermal conditions, reacting $Ni(OH)_2$ with the appropriate organic ligand.[7] This procedure favors a high synthetic control of the reaction, since $Ni(OH)_2$ already contains the metal-hydroxide layers, which undergo cross-linking by the organic ligands with concomitant expansion of the interlayer spacing. Alternatively, a homogeneous self-assembling reaction has been carried out employing $NiCl_2{\cdot}6H_2O$ as starting material, which afforded the MHOFs in the form of nanomaterials composed by only few sheets (called "nanosheets"). These nanostructured MHOFs exhibit an electrochemically active surface area 15 times larger than "bulk" materials prepared from $Ni(OH)_2$,[7] although the extent of synthetic control is much lower than in the latter case. It is worth noting that only the nanosheets were tested for long-term electrochemical stability by Román–Leshkov and Shao–Horn,[15] and investigated by Fisher et al. in the case of NiBDC.[16]

When electron transfer occurs by hopping, the activation of the metal centers prior to the catalytic measurements is required to overcome the energetic barrier arising from the typically low conductance of the organic linkers, increasing the number of catalytic sites. In the literature, a commonly used activation procedure is by CV cycling or by chronoamperometry until a steady state is reached.[18] However, the procedure often disregards a possible evolution of the starting material,[10] which takes place in the case of NiBDC and NiAZO precatalysts.[15,16] In the last years, the literature on these Ni-based MHOFs for OER has become very rich.[7,15,16,19–22] For example, Fisher et al. reported that NiBDC and other Ni-dicarboxylate MHOFs can be

activated by CV cycling until stabilization of the CV curve, which is however sample-dependent.[16] In addition, this activation procedure leads to the complete leaching of the ligands into the KOH solution.

To avoid bias on evaluating the differences in the catalytic performances of NiBDC and NiAZO samples, in this work we propose a possible common activation procedure for these two families of MHOFs, which does not lead to the complete loss of the organic linker and full reconstruction into NiOOH-like phases. $Ni(OH)_2$ (in the β-polymorph phase)[23] was employed as starting material, since the use of bulk and well-defined samples could help the tuning of the MHOF activation procedure. Because $Ni(OH)_2$ itself has been largely studied as a catalyst for OER,[6,24,25] we extended the electrochemical investigation to the starting material as well, since its crystallinity, grain size, structural defects, etc. influence its catalytic properties. Moreover, the aim of this study was also to investigate for the first time the impact of β-$Ni(OH)_2$ crystallinity on MHOF crystallinity, yield, and catalytic activity for OER. Therefore, three samples of β-$Ni(OH)_2$ with low (NiOH-1), intermediate (NiOH-2), and high (NiOH-3) crystallinity were prepared and employed as starting materials to synthesize two families of NiBDC (NiBDC-1, NiBDC-2, and NiBDC-3) and NiAZO (NiAZO-1, NiAZO-2, and NiAZO-3) MHOFs. The MHOFs were deeply characterized with solid state measurements, clarifying some structural aspects that are not much detailed in the literature. Finally, the activation and the electrochemical properties of the Ni^{+2}/Ni^{+3} oxidation and how these can affect the catalytic performances of the MHOFs were studied. Combining CV measurements and ex-situ electronic diffuse reflectance UV–vis–NIR spectroscopy, we investigated the nature of the catalysts at various stages of the process: i) MHOF activation, ii) steady state catalysis, and iii) high-potential catalysis. This allowed us to understand how the chemical surroundings of the Ni centers vary across the catalytic process, evaluating at the same time the chemical and electrochemical stability in alkaline media.[18–20]

2. Results and Discussion

2.1. Solid State Characterizations

$Ni(OH)_2$ is a very interesting material whose physical and chemical properties have been widely studied for many decades, with the aim of tuning them for a wide range of applications.[23] As extensively described in the literature,[23,26–30] β-$Ni(OH)_2$ can be easily obtained in different degrees of crystallinity by tuning the reaction conditions, especially pH of the reaction mixture and aging temperature and time. Here, β-$Ni(OH)_2$ was synthesized by precipitation at room temperature, admixing water solutions of $NiSO_4{\cdot}6H_2O$ and NaOH (~1 M) in 1:4 molar ratio (MR). A twofold molar excess of NaOH was employed to ensure a quantitative precipitation of β-$Ni(OH)_2$, which occurs above pH ~13.[26,29] Moreover, a high pH value was also fundamental to isolate low crystalline β-$Ni(OH)_2$ (NiOH-1) by simple precipitation at room temperature. In fact, at room temperature the α-$Ni(OH)_2$ polymorph can also initially form.[31] However, α-$Ni(OH)_2$ is unstable in strongly basic conditions and rapidly converts into low crystalline β-$Ni(OH)_2$, which is sometimes also denoted as a "badly-crystalline" phase, i.e., β_{bc}-$Ni(OH)_2$.[29] The β-$Ni(OH)_2$ samples with intermediate (NiOH-2) and high (NiOH-3) crystallinity were prepared by hydrothermal treatment, aging NiOH-1 in its supernatant for 24 h at 120 or 180 °C, respectively. The powder X-ray diffraction (PXRD) patterns of the three hydroxides are presented in Figure 2a. In each case the position of the (001) peak indicates an interlayer distance (d_{001}) of 4.6 Å along the *c* axis, which is characteristic of the β-polymorph. In fact, α-$Ni(OH)_2$ possesses a different layered structure, where the hydroxide layers are intercalated by water molecules and SO_4^{2-} ions, yielding a larger interlayer separation. As a consequence of this intercalation, the structure of α-$Ni(OH)_2$ is extremely disordered and possesses very low crystallinity.[23]

As shown by Delmas et al.,[26] the linewidth (LW) of the (001) peak is not sensitive to the number of crystalline defects, since β-$Ni(OH)_2$ only contains stacking faults, which do not introduce misalignments along the *c* axis. On the other hand, misalignments occur in the *ab* plane of the layered structure, which causes a selective broadening of the (10*l*) peaks,[26,32] as shown in Figure 2a for (101) and (102) lines. Therefore, the broadening of the (001) peak moving from NiOH-3 to NiOH-1 is only caused by a decreasing crystallite size.[33] To avoid systematic errors due to the choice of a specific method, the average crystallite size of the three β-$Ni(OH)_2$ samples was evaluated using three different procedures, namely Scherrer formula, Williamson–Hall (W–H) method, and Rietveld refinement (see experimental and ESI for details). Instrumental broadening was taken into account and subtracted prior to the analysis. To obtain the average size of the crystallites using Scherrer formula (Eq. S1), both (001) ($2\theta \sim 19°$) and (101) ($2\theta \sim 38.5°$) reflections were considered, since they possess similar full width at half maximum (FWHM). The shape of the crystallites was assumed to be spherical, using $K = 0.9$ for all three β-$Ni(OH)_2$ samples. The same Bragg peaks were chosen also for the analysis with W–H method. Although W–H approach underestimates the crystallite size of NiOH-3 by ~33%, the three procedures give rewardingly similar results and indicate that the average size of the crystallites increases moving from NiOH-1 to NiOH-3 (Table 1). In particular, we found that NiOH-1 and NiOH-2 possess very small crystallites (≤5 nm), which become much larger only in NiOH-3 (~30 nm). The W–H analysis also highlights that the microstrain decreases from NiOH-1 to NiOH-3, in accordance with literature results.[34] In fact, as crystallinity increases, the misalignment of the layers along the *ab* plane decreases, reducing the number of stacking faults.[26,35] Consequently, the FWHM of the (10*l*) peaks becomes more similar to that of (001) reflections. The morphology of high crystalline NiOH-3 and low crystalline NiOH-1 was analyzed using transmission electron microscopy (TEM), whose results are presented in Figure S1a–c. Compound NiOH-3 is constituted by highly crystalline hexagonal sheets, as expected based on the synthetic conditions employed (Figure S1a).[23] Instead, the TEM images of NiOH-1 (Figure S1b,c) show an almost amorphous material constituted by very small nanosheets, in accordance with the much lower crystallinity of NiOH-3 compared to NiOH-3.

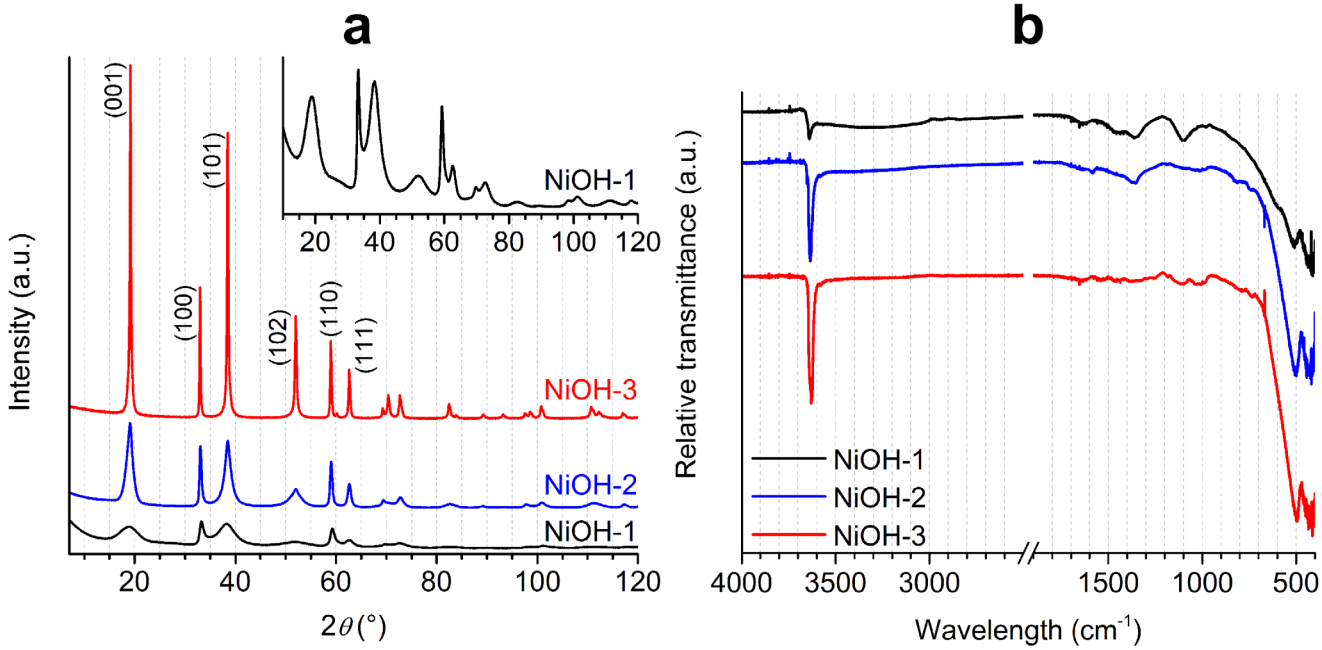

Figure 2. a) PXRD patterns of the three β-Ni(OH)$_2$ samples and indexing of the six most intense peaks (the inset shows a magnification of the pattern of NiOH-1). b) FT-IR spectra of NiOH-1 (top), NiOH-2 (middle), and NiOH-3 (bottom).

Table 1. Calculated average size of crystallites for β-Ni(OH)$_2$ samples (in nm).

Method	NiOH-1	NiOH-2	NiOH-3
Scherrer formula	1.5(4)	4(2)	33(1)
W–H	1.7(2) % Strain = 2.3(1)	4.8(2) % Strain = 0.8(2)	20.8(2) % Strain = 0.001(2)
Rietveld refinement[a)]	1.5(1) R_{wp} = 13.8%	5.0(3) R_{wp} = 11.1%	30.0(5) R_{wp} = 10.8%

[a)] R_{wp} is the weighted profile residual of the Rietveld fit.

The FT-IR spectrum of NiOH-1 is presented in Figure 2b. The narrow band at 3640–3630 cm^{-1} is the stretching ν(OH) band of OH$^-$ groups not involved in H-bonding, typical for β-Ni(OH)$_2$. The presence of OH$^-$ ions is confirmed by the strong band around 510 cm^{-1}, which relates to the δ(NiOH) deformation. In addition, FT-IR spectroscopy indicates the presence of SO_4^{2-} and CO_3^{2-} in NiOH-1, in accordance with the elemental analysis (EA) data in Table 2. In fact, the $\nu(SO_4^{2-})$ modes are found at 1100 cm^{-1} and ~610 cm^{-1} (sh), while $\nu(CO_3^{2-})$ modes are at 1360 and ~1450 cm^{-1} (Figure 2b).[29,36] Low-crystalline β_{bc}-Ni(OH)$_2$, prepared using the same procedure as for NiOH-1, reportedly contains a high percentage of SO_4^{2-} (MR SO_4^{2-}:Ni^{2+} = 0.17),[29] which are adsorbed and bonded to the nickel(II) ions. However, EA (Table 2) indicates that sulfates and carbonates are only present in traces in NiOH-1 (MR SO_4^{2-}:Ni^{2+} = 0.01, MR CO_3^{2-}:Ni^{2+} = 0.03). Therefore, NiOH-1 can be better described as a disordered β-Ni(OH)$_2$ phase with a significant percentage of stacking faults and crystallites of very small average dimensions (see Table 1). Finally, the very broad band centered around ~3300 cm^{-1} relates to ν(OH) of water molecules trapped into the lattice, whose presence is also confirmed by the δ(H$_2$O) bending at 1634 cm^{-1}. The replacement of OH$^-$ groups with H$_2$O molecules is necessary to compensate for the excess of negative charges introduced by SO_4^{2-} and CO_3^{2-} contaminants.[29] The spectra of NiOH-2 and NiOH-3, presented in Figure 2b, show that the ν(OH) and δ(NiOH) bands increase in intensity and slightly shift to lower wavenumbers as crystallinity increases. While residual CO_3^{2-} and H$_2$O molecules are still detected in NiOH-2 (but not in NiOH-3), sulfates are completely replaced by OH$^-$ ions during the alkaline aging process that affords NiOH-2 and NiOH-3, in accordance with EA (Table 2).

These three β-Ni(OH)$_2$ samples were then employed as starting materials in the synthesis of the nickel(II)-based MHOFs, reacting them with H$_2$BDC or H$_2$AZO (Ni:H$_2$L MR = 1.7–1.8:1) in solvothermal conditions (DMF:H$_2$O:EtOH 16:1:1 v/v, 130 °C, 3 days), to give the corresponding NiBDC and NiAZO samples, respectively, (NiOH-1 was used to prepare NiBDC-1 and NiAZO-1, etc…). The PXRD patterns of the products match those reported in the literature[7,37] for NiBDC and NiAZO MHOFs (Figure 3). In particular, both triclinic ($P\bar{1}$) and monoclinic ($C2/m$) phases of NiBDC are present in NiBDC-1, NiBDC-2, and NiBDC-3, as shown in Figure S2. The known crystalline phase (triclinic, $P\bar{1}$) of NiAZO is found

Table 2. Experimental and calculated compositional data (in % m/m) and proposed formulations. For MHOFs samples also the residual quantity of unreacted β-$Ni(OH)_2$ is reported (in % m/m). The last column shows the Brunauer–Emmett–Teller (BET) surface areas.

	C	H	N[a)]	S	Proposed Formulation[b)]	β-$Ni(OH)_2$	BET ($m^2\ g^{-1}$)
$Ni(OH)_2$ calcd.	/	2.17	/	/			
NiOH-1	0.36	2.75	/	0.31	$Ni(OH)_{1.92}(CO_3)_{0.03}(SO_4)_{0.01}{\cdot}0.4H_2O$	/	16
NiOH-2	0.97	2.15	/	/	$Ni(OH)_{1.90}(CO_3)_{0.05}{\cdot}0.1H_2O$	/	73
NiOH-3	0.13	2.13	/	/	$Ni(OH)_2$	/	29
$Ni_2(OH)_2$(BDC) calcd.	30.45	1.92	/	/			
NiBDC-1	26.01	2.41	0.37	/	$Ni_2(OH)_2(BDC){\cdot}0.5Ni(OH)_2{\cdot}0.5H_2O$	12.5	25
NiBDC-2	26.99	2.18	0.17	/	$Ni_2(OH)_2(BDC){\cdot}0.4Ni(OH)_2$	10.5	45
NiBDC-3	30.42	2.20	0.20	/	$Ni_2(OH)_2(BDC)$	/	43
$Ni_2(OH)_2$(AZO) calcd.	40.07	2.40	6.68	/			
NiAZO-1	19.67	2.61	3.25	/	$Ni_2(OH)_2(AZO){\cdot}4.5Ni(OH)_2{\cdot}H_2O$	48.8	13
NiAZO-2	38.52	2.67	6.23	/	$Ni_2(OH)_2(AZO){\cdot}0.2Ni(OH)_2$	4.2	32
NiAZO-3	38.64	2.80	6.29	/	$Ni_2(OH)_2(AZO){\cdot}0.15Ni(OH)_2$	3.2	40

[a)] Residual nitrogen in NiBDC samples is due to traces of trapped DMF;
[b)] Calculated compositional data for the proposed formulations can be found in the experimental section.

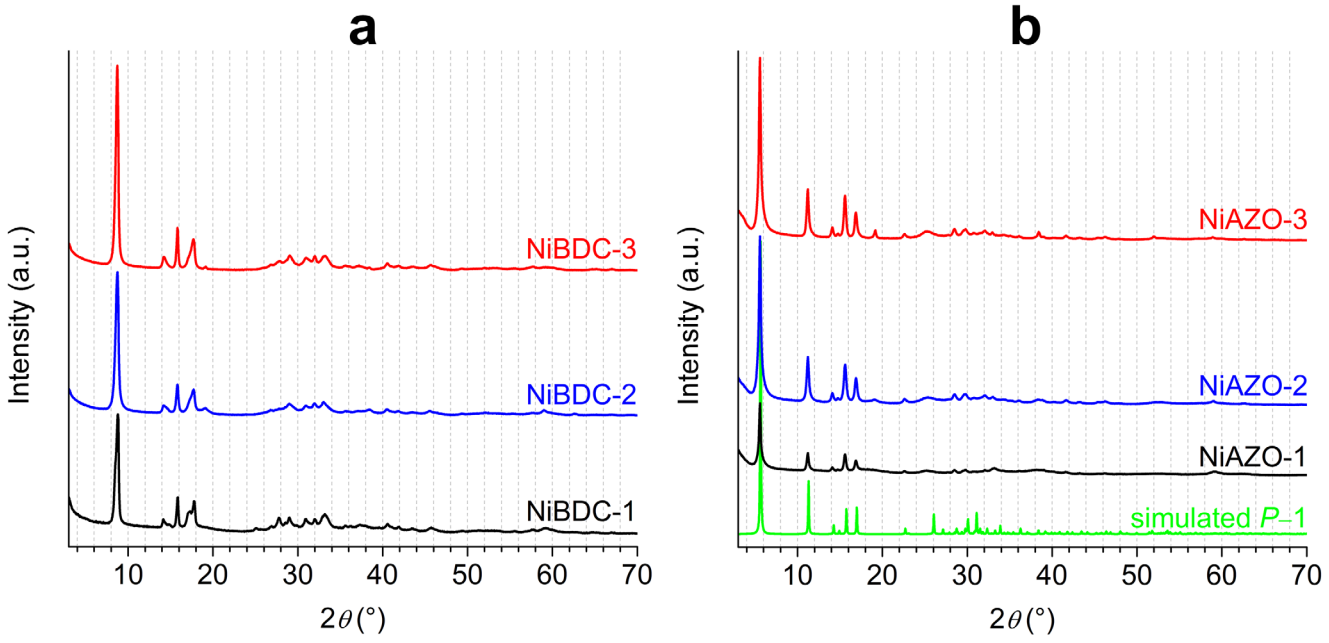

Figure 3. Experimental PXRD patterns of a) NiBDC and b) NiAZO samples. Panel b also presents the simulated pattern of NiAZO.

in NiAZO-1, NiAZO-2, and NiAZO-3. The presence of residual β-$Ni(OH)_2$ in each NiL sample is clearly highlighted by the peak around $2\theta = 19°$ in the PXRD patterns, as shown in Figure 3 (see Figures S3 and S4 for expanded views). Compositional data of NiL samples (Table 2) indicate that the amount of residual β-$Ni(OH)_2$ decreases from NiL-1 to NiL-3, suggesting that the intercalation reaction is more effective when highly crystalline β-$Ni(OH)_2$ is employed. Interestingly, the PXRD patterns within the same family of NiL MHOFs are very similar, indicating that the degree of crystallinity of the final product is unrelated to that of the β-$Ni(OH)_2$ precursor. On the other hand, the crystallinity of unreacted β-$Ni(OH)_2$ seems to mirror that of the precursor. Therefore, these results suggest that the intercalation of BDC^{2-} and AZO^{2-} organic linkers removes the disorder between the layers in low crystalline β-$Ni(OH)_2$, affording highly crystalline MHOFs.

A detailed investigation on phase composition was then performed through quantitative phase analysis (QPA) of the PXRD patterns using Rietveld refinement, whose results are gathered in Table 3 and in Figures S5–S13 (details on the Rietveld fits can be found in the ESI). Moreover, since PXRD is a bulk technique only sensitive to crystalline phases, the relative quantities of the phases obtained using QPA (Table 3) were compared with those resulting from EA (Table 2). In all cases, QPA confirms that the residual β-$Ni(OH)_2$ preserves its initial crystallinity and average crystallite size, which are therefore not influenced by the

Table 3. Phase composition of the MHOF samples (in % m/m) and R_{wp} of the Rietveld refinements.

Sample	NiBDC		NiAZO	β-Ni(OH)$_2$	R_{wp} (%)
	C2/m	$P\bar{1}$	$P\bar{1}$	$P\bar{3}m1$	
NiBDC-1	69(2)	19.6(9)	/	11.4(5)	11.4
NiBDC-2	77.9 (3)	14.2(1)	/	7.9(3)	11.3
NiBDC-3	71.0(2)	27.2(1)	/	1.8(1)	14.3
NiAZO-1	/	/	50.5(3)	49.5(1)	10.1
NiAZO-2	/	/	94.6(2)	5.4(3)	13.4
NiAZO-3	/	/	96.0(2)	4.0(3)	13.1

employed solvothermal conditions. The residual quantities of β-Ni(OH)$_2$ in the NiL samples calculated by QPA (Table 3) are in very good agreement with those estimated by EA (Table 2), confirming that highly crystalline precursors are more easily intercalated by L^{2-}. In particular, the intercalation is much less effective in the case of NiAZO-1, since the isolated powder contains ~50% by weight of the β-Ni(OH)$_2$ precursor (Tables 2 and 3). This could be ascribed to the lower ligand concentration used to synthesize the NiAZO samples compared to the NiBDC ones (see experimental section), or to a higher activation barrier of the intercalation reaction for the longer AZO^{2-} linker. However, these effects are only relevant when low crystalline NiOH-1 is used, since these differences are not evident within the NiL-2 and NiL-3 families. These findings thus suggest that the biggest impediment to the intercalation of L^{2-} is the energy required to remove stacking faults disorder in low-crystalline NiOH-1, and that this energy is lower for BDC^{2-} compared to the longer AZO^{2-} linker.

Finally, the average crystallite size of the MHOF samples was also estimated, to demonstrate that their crystallinity does not significantly depend on that of the employed β-Ni(OH)$_2$ precursor. On NiBDC samples, the analysis through Rietveld refinement was complicated by the copresence of both monoclinic and triclinic phases, and by the low angular resolution of the PXRD patterns. Therefore, the estimation was based on the application of Scherrer equation (Equation S1) to the peak at $2\theta = 15.8°$, which is common to both crystal phases. Setting $K = 0.9$, we obtained similar crystallite sizes for NiBDC-1, NiBDC-2, and NiBDC-3 [57(3), 57(2), and 53(3) nm, respectively]. Similar conclusions were drawn for the NiAZO samples. In this case, the calculations were more reliable since both Scherrer equation [$K = 0.9$, applied to the peaks at $2\theta = 5.56°$, 11.20°, and 15.58°, corresponding to the (100), (200), and (110) reflections, respectively] and Rietveld refinement were applicable. Both methods provided similar average crystallite sizes for NiAZO-1, NiAZO-2, and NiAZO-3, namely 35(3), 30(2), and 38(3) nm using Scherrer method, and 40(3), 35(2), and 34(2) nm using Rietveld refinement. Finally, the morphology of the MHOFs was characterized analyzing NiBDC-3 and NiAZO-3 with TEM. The TEM images in Figures S1d–f and S14d–f confirmed that both MHOFs are constituted by sheets of variable dimensions, similar to what reported in the literature.[7,15] In conclusion, this detailed compositional analysis demonstrates that the intercalation of the organic L^{2-} ligands into β-Ni(OH)$_2$ effectively removes stacking faults defects (if present), leading to an increased crystallite size and affording highly crystalline MHOFs. Therefore, the stabilization energy due to intercalation is higher than the energy required to remove the misalignment along the planes of β-Ni(OH)$_2$.

The FT-IR spectra of NiBDC-1, NiBDC-2, and NiBDC-3 are very similar to each other (Figure 4a). Interestingly, three narrow ν(OH) bands of non-hydrogen bonded OH^- groups are found at 3610, 3591, and 3526 cm^{-1}. Comparison with the spectrum of a sample of Ni$_2$(OH)$_2$(BDC) prepared starting from NiCl$_2$·6H$_2$O and containing prevalently the triclinic form (NiBDC*a* in Figure S15) allowed to assign the band at 3610 cm^{-1} to the monoclinic phase, and the other two weaker bands to the triclinic form. To further support our assignments, an isotopically enriched analogue of NiBDC*a* containing almost exclusively the triclinic phase, Ni$_2$(OD)$_2$(BDC) (NiBDC*a*-d_2), was prepared working in a DMF:D$_2$O solvent mixture. Its FT-IR spectrum (Figure S15) shows weak residual ν(OH) bands, with the peaks at 3591 and 3526 cm^{-1} being much more intense than that at 3610 cm^{-1}. The same pattern is observed for ν(OD) bands at 2663, 2650, and 2603 cm^{-1}. Rewardingly, the isotopic shift factor is the same for each band ($\nu_{OH}/\nu_{OD} = 1.355$–$1.356$) and in perfect accordance with that of non-hydrogen bonded OH^- ions.[38] One intriguing result is the observation of two ν(OH) bands with ~1:1 relative intensity in the triclinic phase. Because both phases (monoclinic and triclinic) contain a single OH^- group in the asymmetric unit, only one ν(OH) band would be expected, as indeed found for the monoclinic phase. The possible occurrence of two inequivalent OH^- ions in the triclinic phase indicates that its reported structure may require revision.

In the three NiBDC samples, the broad band centered around 3300–3200 cm^{-1} (Figure 4a) is indicative of residual (noncoordinating) water molecules, in accordance with compositional data (the experimental percentages of H are higher than the theoretical ones). The complete absence of the ν(C═O) vibration at ~1700 cm^{-1} implies that the organic ligand is fully deprotonated. Metal coordinated carboxylates give rise to the strong bands at ~1580 and ~1350 cm^{-1}, assigned to the asymmetric (ν_{as}) and symmetric (ν_s) stretching modes of the COO^- group. The weak band at 1498 cm^{-1} is attributed to aromatic semi-circle stretching mode ν(C—C), while the shoulder at 827–825 cm^{-1} is the out-of-plane deformation of the two adjacent aromatic CH. Finally, the strong and medium bands at 813–811 cm^{-1} and 688–685 cm^{-1} are the in-plane and out-of-plane deformations of bridging OH^- ligands (which in fact are considerably weakened in NiBDC*a*-d_2).

The FT-IR spectra of the NiAZO samples (Figure 4b) are very similar to each other and share many bands with those of the NiBDC samples. On the other hand, some differences stand out clearly, namely: i) only one ν(OH) band attributable to non-hydrogen bonded OH^- groups is found at 3613 cm^{-1}, in accordance with the reported molecular structure for NiAZO, where all the OH^- ions are equivalent; ii) the aromatic quadrant stretching mode ν(C—C) at 1598 cm^{-1} is here an IR-active mode, while it is inactive in symmetrically *para*-disubstituted rings (such as in BDC^{2-}); iii) the wavenumber separation ($\Delta\nu$) between $\nu_{as}(COO^-)$ and $\nu_s(COO^-)$ is 194 cm^{-1}, hence lower than in NiBDC samples (227–228 cm^{-1}). The $\Delta\nu$ parameter is widely used in the literature to establish the coordination mode of

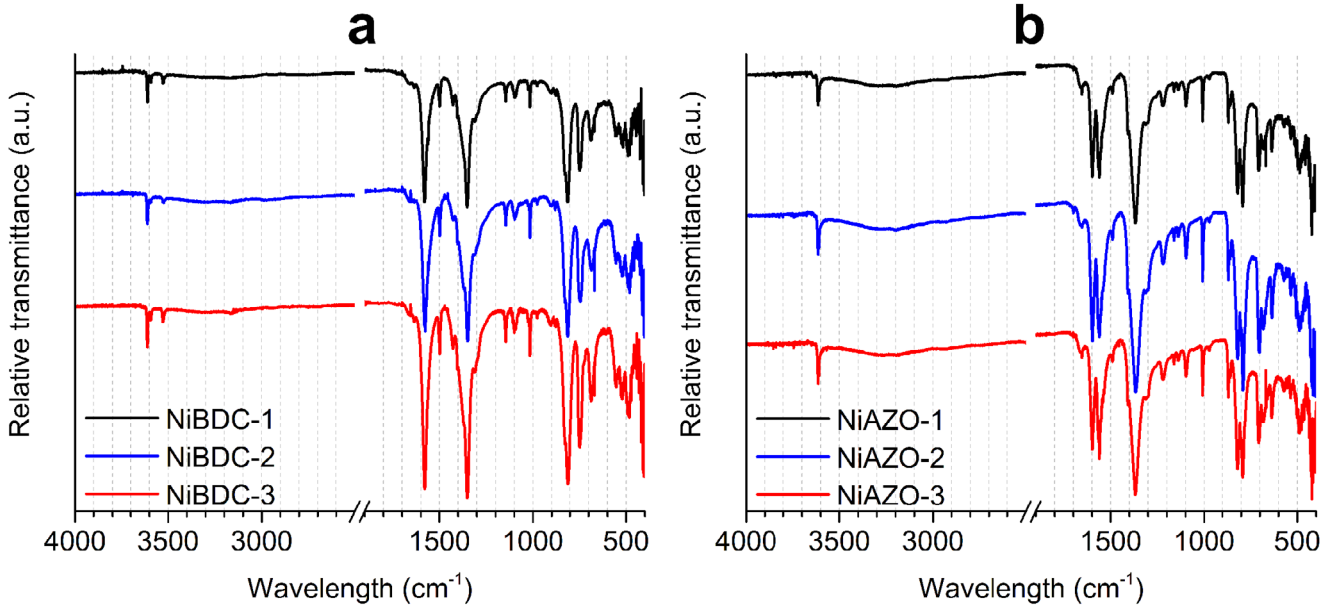

Figure 4. a) FT-IR spectra of NiBDC-1 (top), NiBDC-2 (middle), and NiBDC-3 (bottom). b) FT-IR spectra of NiAZO-1 (top), NiAZO-2 (middle), and NiAZO-3 (bottom). The weak band at ~1660 cm^{-1} is the ν(C=O) of residual DMF traces.

carboxylates with unknown structure.[39,40] In particular, a high value of $\Delta\nu$ (i.e., >180 cm^{-1}) is often associated to monodentate carboxylates, whereas a bridging coordination is usually related to lower values of $\Delta\nu$ (e.g., 160–170 cm^{-1} for acetates). However, in the structures of NiBDC[7,37,41] and NiAZO[7] each carboxylate coordinates three nickel(II) ions in a *syn/syn*, *syn* bridging mode as depicted in Figure S16. This result supports the idea that the above described criterium does not have general validity and that $\Delta\nu$ is an empirical parameter that needs to be used with care.[40,42]

The solid-state UV–vis–NIR diffuse reflectance spectra of β-$Ni(OH)_2$, NiBDC, and NiAZO samples are presented in Figure 5. Within the same family of samples, the spectra are very similar to each other, while spectral resolution increases as crystallinity increases (Figure 5a–c). Six-coordinate octahedral nickel(II) ions display three spin-allowed transitions from the ground $^3A_{2g}(F)$ term to the excited ones: $\nu_1 = {}^3A_{2g}(F) \rightarrow {}^3T_{2g}(F)$, $\nu_2 = {}^3A_{2g}(F) \rightarrow {}^3T_{1g}(F)$, and $\nu_3 = {}^3A_{2g}(F) \rightarrow {}^3T_{1g}(P)$.[43] For example, the β-$Ni(OH)_2$ samples (Figure 5a) show ν_1 at ~1135–1150 nm (very broad), while ν_2 (~670 and 745 nm), and ν_3 (~390 and 420 nm) are clearly split by deviations from octahedral symmetry. In fact, the nickel(II) ions in β-$Ni(OH)_2$ possess D_{3d} symmetry imposed by the trigonal space group ($P\bar{3}m1$), which splits the T_{1g} terms into $A_{2g} + E_g$ (the splitting of the very broad ν_1 band is not resolved).[44] These transitions cannot be assigned directly, since spin-orbit coupling can also contribute to the splittings, scrambling the position of the A_{2g} and E_g terms.[43] In the spectra of the NiBDC and NiAZO MHOFs (Figure 5b,c), ν_3 is hidden by charge-transfer and/or $\pi \rightarrow \pi^*$ bands arising from the organic ligand, while ν_2 and ν_1 transitions appear similar to those of β-$Ni(OH)_2$ (Figure 5d). Therefore, UV–vis–NIR spectroscopy confirms that all the analyzed samples contain nickel(II) in distorted octahedral geometry, as expected from literature structural data.[7,37]

At higher wavelengths, the two absorptions around ~1380 (~7246 cm^{-1}) and ~1415–1425 nm (~7067–7018 cm^{-1}) are assigned to combination bands of free OH^- stretchings.[45] A third band is present at 1452 nm (6887 cm^{-1}) in the spectra of NiBDC samples. Interestingly, this band and that at ~1420 nm are the only ones present in this region in the spectrum of triclinic NiBDC*a* (Figure S17). In NiBDC*a*-d_2, they are both shifted to higher wavelengths by the same isotopic shift factor = 1.35 (Figure S17). This result further supports our previous hypothesis that the triclinic form of NiBDC contains two non-equivalent OH^- ions, in contrast with the reported structure.[7] Less energetic transitions around ~1665 nm (absent in β-$Ni(OH)_2$ samples) and at $\lambda > 1900$ nm are assigned to combination bands and overtones of IR modes with possible contributions from the linkers (Figure 5d).[46]

X-ray absorption near-edge structure (XANES) data for β-$Ni(OH)_2$, NiBDC, and NiAZO samples at the O K- and Ni L-edges are presented in Figures 6 and 7, respectively. The features in Figure 6 come from O1s→ O2p transitions, where the O2p orbitals are hybridized with the metal ones. In particular, in other metal oxides the features around 530 eV are commonly ascribed to transitions where the O2p orbitals are hybridized with the 3d orbitals of the metal, whereas those in the 536–543 eV range are assigned to O2p orbitals hybridized with the 4s and 4p orbitals of the metal.[47] For the β-$Ni(OH)_2$ samples, the intensity and resolution of the spectra depend markedly on crystallinity. In particular, the peak at ~534 eV becomes broader as crystallinity decreases, very likely due to the more pronounced inhomogeneous broadening expected in more disordered structures.[48] On the other hand, the spectra within the NiBDC and NiAZO families are very similar, in accordance with the fact that the crystallinity of the MHOFs is similar within each family. However, the spectra of the MHOFs strongly differ from those of the β-$Ni(OH)_2$ samples (Figure 6), in agreement with the different

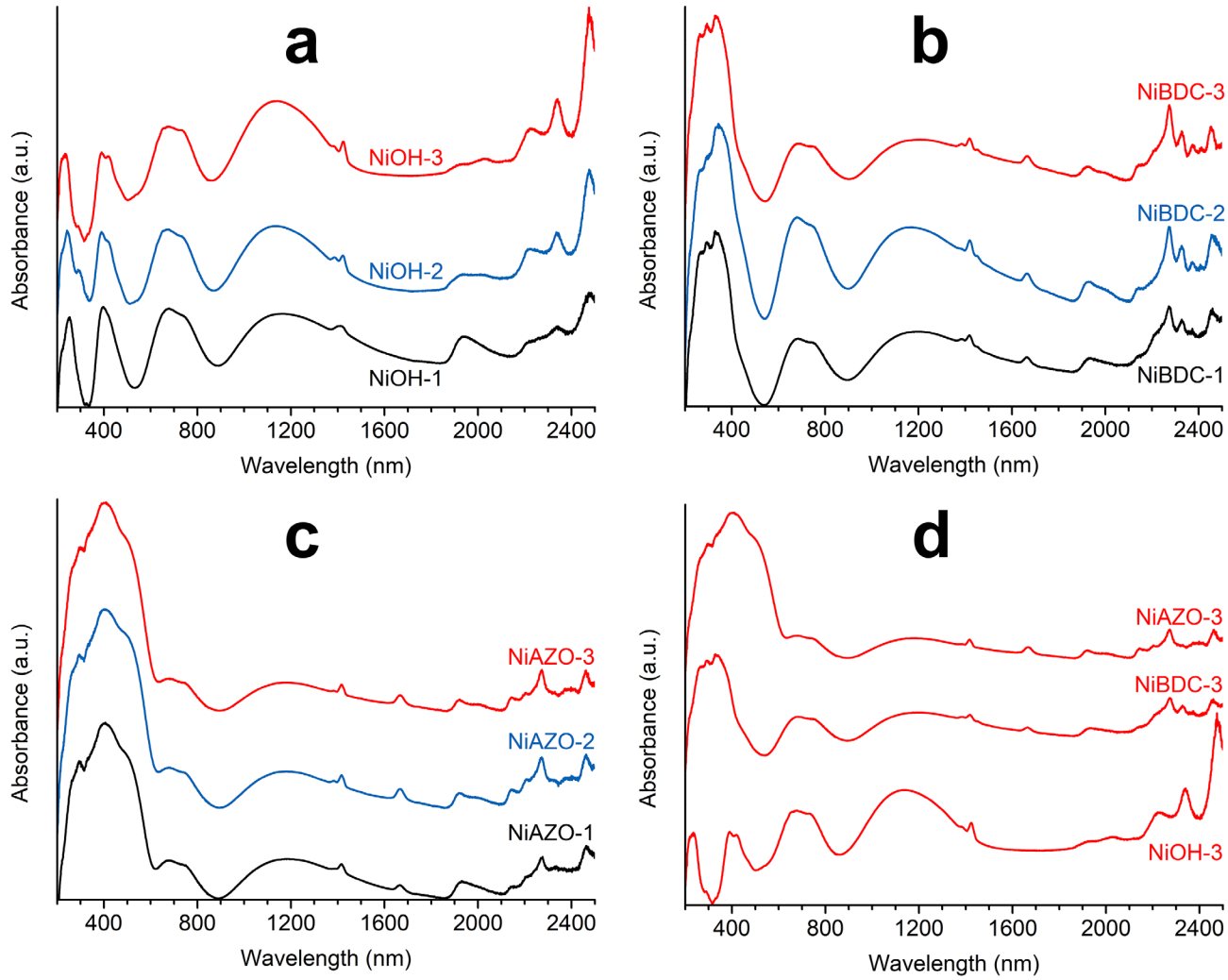

Figure 5. Solid-state diffuse reflectance UV–vis–NIR spectra of a) β-Ni(OH)$_2$, b) NiBDC, and c) NiAZO samples. Panel d) compares the spectra recorded on the three samples with high crystallinity.

nature of the oxygen donors. At the Ni L-edges (Figure 7), the signals arise from the 2p→3d dipole transitions. The observed features originate from atomic multiplet effects and are sensitive to the oxidation state of the Ni sites, their local geometry, and symmetry.[49] Noticeably, the Ni L-edge XANES spectra are similar for all the samples, with no detectable dependence on crystallinity in samples of β-Ni(OH)$_2$. This result confirms that all the samples contain only nickel(II) ions with very similar coordination geometry, in accordance with diffuse reflectance UV–vis–NIR spectroscopy (Figure 5), and in good agreement with XAS Ni K-edge measurements reported by Fisher et al. on NiBDC and other Ni-dicarboxylate MHOFs.[16] Moreover, the spectra presented in this work perfectly match those in the literature, where a wide consensus has been reached on the features at the Ni $L_{3,2}$-edges and their intensity ratio in Ni(OH)$_2$.[49–51] As an exception, in the spectrum of β-Ni(OH)$_2$ reported by Samarai and coworkers the two features at the L_3-edge possess the same intensity.[52] Being this the only spectrum collected in Total Fluorescence Yield (TFY) mode, the anomaly is very likely due to self-absorption effects, which also affect our TFY spectra, although to a minor extent (Figure S18).

2.2. Electrochemistry

The electrochemical properties of β-Ni(OH)$_2$, NiBDC, and NiAZO samples were investigated through CV in 0.1 M aqueous KOH. All the electrochemical measurements were performed at a higher scan rate (50 mV s^{-1}) than the one usually proposed in the literature (10 mV s^{-1}) since, in the absence of a rotating electrode, the formation of bubbles at catalytic potentials affects the result of the CV measurement. Therefore, on each sample we firstly performed 10 CV cycles at 50 mV s^{-1} from +0.96 V to +2.46 V versus RHE, as shown in Figures S19–S21. For all the materials, the anodic scan of the 1st CV cycle shows a first poorly defined signal, with shoulder shape, due to the oxidation of Ni^{2+} to Ni^{3+} (signal Ia). A second much more intense signal (signal IIa), with a roughly sigmoidal shape, is due to the oxidation of water to O_2 during OER (gas bubbles were indeed observed on the working electrode in this potential region). The cathodic return consists of a barely visible, broad, and low-current single signal (signal Ic) at a less positive potential than signal Ia. It corresponds to the counterpart of signal Ia and can be confidently assigned to Ni^{3+}→Ni^{2+} reduction. The CV responses for these experiments showed that,

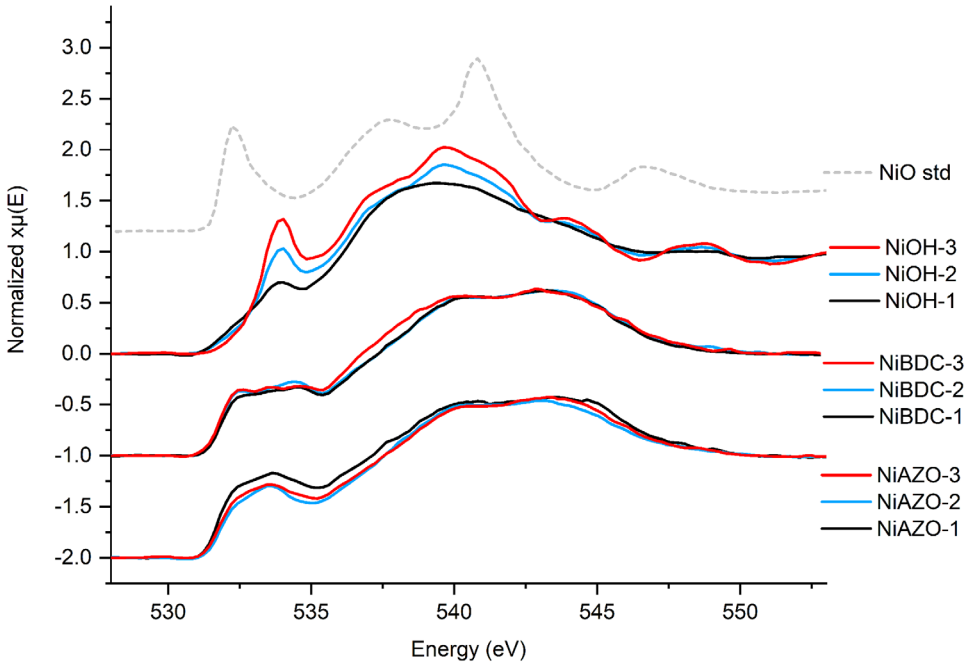

Figure 6. Normalized O K-edge total electron yield (TEY) XANES spectra of β-Ni(OH)$_2$, NiBDC, and NiAZO samples. For reference, also the spectrum of NiO (top, grey dashed line, with intensity rescaled by a 0.5 factor) from the beamline database is reported.

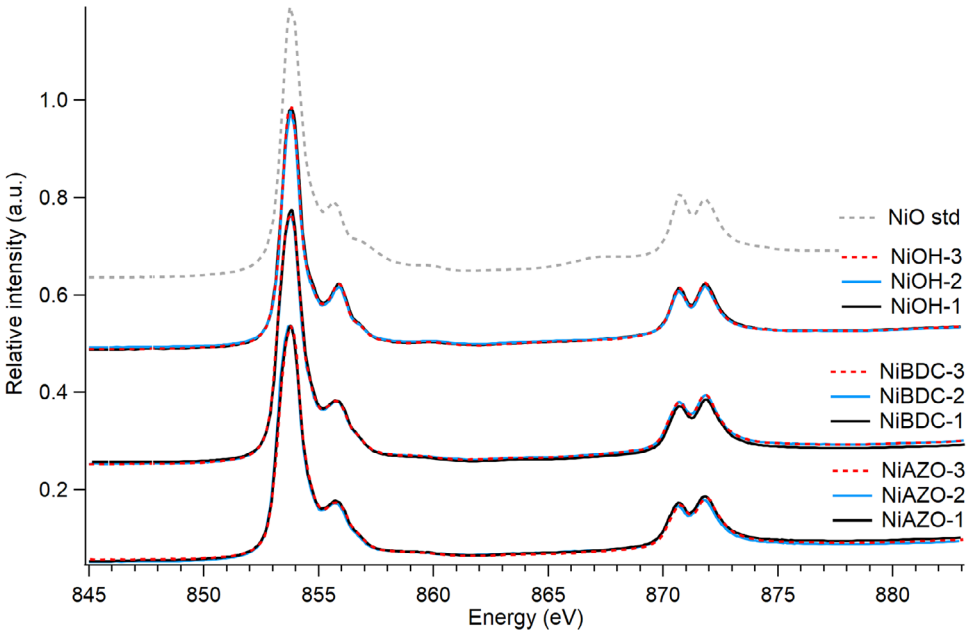

Figure 7. Normalized and background subtracted Ni L-edge TEY XANES spectra of β-Ni(OH)$_2$, NiBDC, and NiAZO samples. For reference, also the spectrum of NiO (top, grey dashed line) taken from the beamline database is reported. The alignment of the energy scale and the shape of all the spectra match well with those previously reported for Ni(OH)$_2$.[49]

during the first 5–6 cycles, both the Ni^{2+}/Ni^{3+} redox signals (Ia and Ic) and the OER signal (IIa) were completely quenched (see Figures S19–S21).

As already reported for NiBDC and NiAZO nanosheets (synthesized in homogeneous conditions from $NiCl_2$),[15,16] the structural evolution during the electrochemical measurements seems to be strongly influenced by the exposure to the electrolyte and the conversion to NiOOH-like phases that takes place at positive potentials. In addition to the potential dependent-evolution of the catalysts, extensive formation of bubbles was noticed at potentials higher than +1.7 V, possibly leading to the gradual removal of the deposited material from the glassy carbon (GC) surface and/or the passivation of the latter.[53] Therefore, the loss of the electrochemical signal of all the tested catalysts during CV cycling with an endpoint (ep) potential of +2.46 V (ep10) could reflect a combination of competing and destructive processes happening on the GC surface.

Table 4. Summary of the different potential ranges and cycles used during CV measurements.

CV cycle number	Potential Range (in V versus RHE)	Endpoint
1 – 40	+0.96/+1.56	ep1
41 – 50	+0.96/+1.66	ep2
51 – 60	+0.96/+1.76	ep3
61 – 70	+0.96/+1.86	ep4
71 – 80	+0.96/+1.96	ep5
81 – 90	+0.96/+2.06	ep6
91 – 100	+0.96/+2.16	ep7
101 – 110	+0.96/+2.26	ep8
111 – 120	+0.96/+2.36	ep9
121 – 130	+0.96/+2.46	ep10

To further investigate the effect of the applied potential on the electrochemical stability of our catalysts, other CV experiments were performed, in which the endpoint potential was progressively increased in steps of 100 mV from +1.56 V (ep1) to +2.46 V (ep10), as summarized in Table 4.

Figure 8 shows the 1st and the 40th (steady state) CV cycles, with endpoint potential of +1.56 V (ep1), recorded on the high crystallinity samples NiOH-3, NiBDC-3, and NiAZO-3. For NiOH-3 sample (Figure 8a), the repeated CVs at ep1 induce an increase of the current for both Ia and Ic signals, which progressively become well shaped and stable in terms of both potential and current. Although for NiBDC-3 and NiAZO-3 repeated CV cycles at ep1 still give rise to stable and well-defined signals, the anodic and cathodic currents do not increase (Figure 8b,c). Upon shifting the endpoint potential to ep2 (+1.66 V), repeated CVs show a further increase in the current limit of Ia and Ic for NiOH-3. The increment in current at ep2 is observed also for NiBDC-3, while under the same conditions, the CVs of NiAZO-3 do not change significantly. The described trends within each family of materials are observed also for NiOH-1, NiOH-2, NiL-1, and NiL-2 samples, as shown in Figure S22.

The observation of larger current signals for the Ni^{2+}/Ni^{3+} redox process upon repeated cycling indicates an increase of the number of Ni sites available for electron transfer, in accordance with what reported in the long-term stability measurements of the MHOF nanosheets.[15] For the β-$Ni(OH)_2$ and NiBDC samples, the gradual increment of the endpoint potential leads to a further increase in the number of available catalytic centers as shown in Figure S23. However, in general, when the endpoint is above +1.96 V (ep5), Ia, Ic, and IIa signals show a progressive drop in current until they completely disappear (Figure S24), confirming that the electrochemical stability depends on the potential range, even after the stabilization of the signals by the previous CV cycling (from ep1 to ep5). On the other hand, the NiAZO samples reach their steady states at lower endpoint potential (ep1), and Ia, Ic, and IIa signals do not decrease until cycling at ep7, suggesting a higher stability. This result is consistent with the behavior of MHOF nanosheets, with NiBDC undergoing a full reconstruction into NiOOH-like phases while this transformation is only superficial for NiAZO.[15] Notably, a significant loss of signal occurs at higher potentials for NiOH-3 (around ep8/ep9, see Figure S24g) than for NiOH-1 and NiOH-2 (Figure S24a,d), indicating that more crystalline samples have enhanced electrochemical stability. The same trend is however observed also for the NiBDC samples (Figure S24b,e,h), that possess similar crystallinity, suggesting that their electrochemical stability also depends on the crystallinity and/or amount of residual unreacted β-$Ni(OH)_2$. In contrast, these differences are not observed within the NiAZO samples, due to their higher intrinsic stability. However, this result is unexpected for NiAZO-1, since it contains ~50% in weight of unreacted NiOH-1 (see Table 3), which is the less stable material. What has been observed with CV cycling at potential higher than ep5 was also confirmed by chronopotentiometry measurements (Figure S25). The potential exhibited by NiOH-3 and NiBDC-3 does not change significantly when a current density (J) of 10 mA cm^{-2} is applied for 2 h, confirming high stability under OER conditions. Instead, for NiAZO-3 a moderate but progressive increase in potential is observed during the first 40 minutes at J = 10 mA cm^{-2}. However, the applied J is much higher than what has been tested by

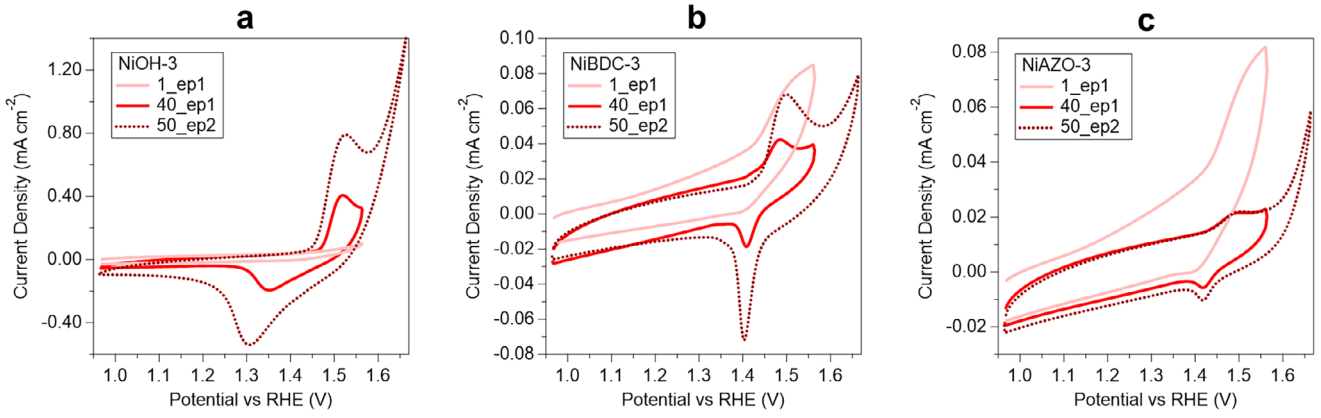

Figure 8. 1st and 40th CV cycles in the potential range +0.96/+1.56 V versus RHE (1_ep1 and 40_ep1), and 10th CV cycle in the potential range + 0.96/+1.66 V versus RHE (50_ep2) recorded on the NiOH-3 (a), NiBDC-3 (b), and NiAZO-3 (c) catalysts. Scan rate = 0.05 V s^{-1}, T = 25 °C, in 0.1 M KOH.

Yuan et al. who found that NiAZO is stable at $J = 0.05$-1 mA cm^{-2} for 50 min.[7]

Recently very detailed studies describing the mechanism of activation and the long-term stability of NiBDC and NiAZO nanosheets were reported.[15,16] However, to the best of our knowledge a common activation procedure to evaluate differences in the catalytic activities of NiBDC and NiAZO for OER has yet to be established. Our results suggest that a convenient, simple, and reproducible activation protocol for all materials consists in cycling up to ep4 (40 CVs at ep1, plus 10 CVs at ep2, plus 10 CVs at ep3, plus 10 CVs at ep4), since this potential (+1.86 V) affords the maximum production of NiOOH-like active phase without current drops, which occur at higher potentials (>ep5). An alternative activation procedure based on chronoamperometry (CA) was also tested for comparison for NiOH-3, NiBDC-3, and NiAZO-3, and the results are presented in Figure S26. A potential of +1.6 V (versus RHE) was chosen because it follows the Ni^{2+}/Ni^{3+} redox process (Ia) and is about ~5 mV lower than the onset potential of the OER (IIa). The CA potential was applied for 32 min, which corresponds to the time required for the proposed activation by CV cycling (CV-activation). This is a key point since Zheng et al. reported that for NiBDC and NiAZO the exposure time to the 0.1 M KOH solution has a stronger impact on the transformation of the MHOFs than the applied potential.[15] Figure S26 shows that in all cases the two different activation methods lead to similar CV response. Some minor differences can be observed only for the Ni^{2+}/Ni^{3+} redox signal (Ia), while the catalytic currents are very similar. However, it has to be considered that CV-activation allows a direct comparison with literature data on NiBDC and NiAZO, since they were mainly activated by CV cycling.[7,15,21] Moreover, CV is more informative than CA since it allows to directly probe the evolution of the redox properties of the metal center during the experiment, and to correlate the observed variations with the catalytic response.

As a support to the proposed activation procedure, we tested the electrochemical stability of β-Ni(OH)$_2$, NiBDC, and NiAZO samples during the process to understand if the reconstruction into NiOOH-like phases is only superficial or bulky. Thus, NiOH-3, NiBDC-3, and NiAZO-3 were studied as function of CV cycling at different endpoints using diffuse reflectance UV–vis–NIR spectroscopy, as presented in Figure 9. The spectra were collected on samples freshly deposited on the electrode (spectrum A), after 40 CVs at ep1 (spectrum B), after 40 CVs at ep1 plus 10 additional cycles at ep4 (spectrum C), and after 40 CVs at ep1 plus 10 additional cycles at ep8 (spectrum D). For all samples, no significant variations were detected between spectra A and B, indicating that cycling in the potential window of the Ni^{2+}/Ni^{3+} redox process does not affect the materials. When NiOH-3 is cycled at ep4 (Figure 9a, spectrum C) a new very broad band appears, indicating a bulk reconstruction of β-Ni(OH)$_2$ into NiOOH-like phases (see spectra E and F in Figure 9a). Therefore, although in this potential window the catalytic signal of NiOH-3 remains stable (see Figure S23c), the sample undergoes partial degradation, which becomes even more significant at ep8 (Figure 9a, spectrum D). On the other hand, the spectra of NiBDC-3 and NiAZO-3 remain unvaried after cycling at ep4 (Figure 9b,c, spectra C), indicating higher electrochemical stability. Therefore, we suggest that the activation procedure proposed in this work (i.e., cycling from ep1 to ep4) does not affect the bulk composition of the MHOFs while at the same time it is efficient enough to produce the NiOOH-like active phase on the surface of each catalyst (see above). Spectrum D of NiBDC-3 (Figure 9b) does not show significant variations, in accordance with the fact that a complete loss of signal is observed only at ep9 (see Figure S24h). NiAZO-3 behaves similarly and spectrum D indicates that bulk reconstruction into NiOOH-like phases is marginal even at ep8.

For all the samples (regardless of their degree of crystallinity), the intensity of Ia and Ic and their potential value are constant after the first 40 cycles (ep1), indicating a quasi-reversible oxidation/reduction Ni^{2+}/Ni^{3+} process (Figure 8). Under these conditions, the $E^{0\prime}$ of the redox reaction can be calculated as the semi-sum of the anodic (E_{Ia}) and cathodic (E_{Ic}) peak potentials ($E^{0\prime}$ values are listed in Table S1). The peak-to-peak separation ($\Delta E_p = E_{Ia} - E_{Ic}$), a parameter related to the electron transfer rate, is ~2–2.5 times larger for β-Ni(OH)$_2$ than for NiBDC and NiAZO samples, indicating that a more efficient electron transfer occurs in the MHOFs. Moreover, the peak current of Ia is linear with the square root of the scan rate, revealing that this electron transfer process is diffusion-controlled (Figure S27). These results suggest that the diffusion of negative ions, needed to compensate for the increased positive charge during oxidation, is slower inside the β-Ni(OH)$_2$ samples.[24]

The sharp current increase observed at potentials higher than +1.60 V is due to the OER, as already reported for NiBDC and NiAZO.[7] At +1.80 V, the currents are from 2 to 30 times larger (depending on the sample) than those recorded on the bare GC electrode. The OER catalytic performances of all samples were evaluated through linear sweep voltammetry (LSV) as shown in Figure 10a–c, and the results are gathered in Table 5. In particular, we determined the overpotential (η) at 1 mA cm^{-2} (equal to $E_{OER} - 1.23$ V, where E_{OER} is the potential at 1 mA cm^{-2}), the onset potential (E_{onset}), the slope of the Tafel plot (Figure 10d–f), and the J value at +1.80 V, as graphically shown in Figure 11. The catalytic parameters (η_{CAT}, $E_{OER,CAT}$, Tafel slope) were evaluated from the catalytic current densities (J_{CAT}) obtained subtracting the contribution of the Ni^{2+}/Ni^{3+} oxidation from the total J (see Figure S28). Before running LSV, the electrodes coated with the catalyst powder were subjected to the above presented activation procedure, consisting in CV cycling from ep1 to ep4. Neither the studied catalysts nor the bare GC electrode reached $J = 10$ mA cm^{-2} (usually taken as a benchmark value in the literature) within the measured potential window. Therefore, η_{CAT} was evaluated at $J = 1$ mA cm^{-2} (see Table 5).

The results show that NiOH-3 exhibits the lowest OER overpotential of 455 mV. Instead, η_{CAT} of MHOF samples and of the bare electrode (GC), obtained under identical conditions, are always higher than 550 mV and 700 mV, respectively. Figure 10d–f presents the Tafel plots obtained from LSV curves to assess OER kinetics on the modified electrodes (the corresponding slopes are reported in Table 5). The Tafel slopes amount to ~84 mV dec^{-1} for all β-Ni(OH)$_2$ samples, while they range between 78 mV dec^{-1} and 92 mV dec^{-1} for the NiBDC samples, and between 64 mV dec^{-1} and 71 mV dec^{-1} for the NiAZO ones. Therefore, NiAZO samples exhibit the highest catalytic performance, along

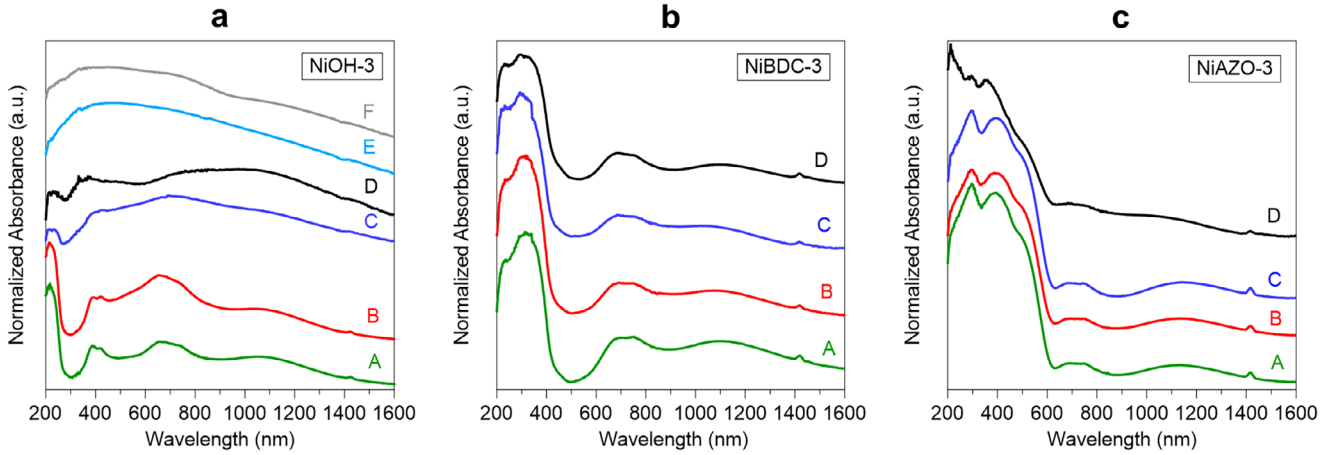

Figure 9. Diffuse reflectance UV–vis–NIR spectra of a) NiOH-3, b) NiBDC-3, and c) NiAZO-3 immobilized on the electrode recorded: before CV cycling (A), after 40 cycles at ep1 (B), after 40 cycles at ep1 and 10 cycles at ep4 (C), and after 40 cycles at ep1 and 10 cycles at ep8 (D). In addition, the spectra of βb-NiOOH (E) and γ-NiOOH (F) are reported in panel a.

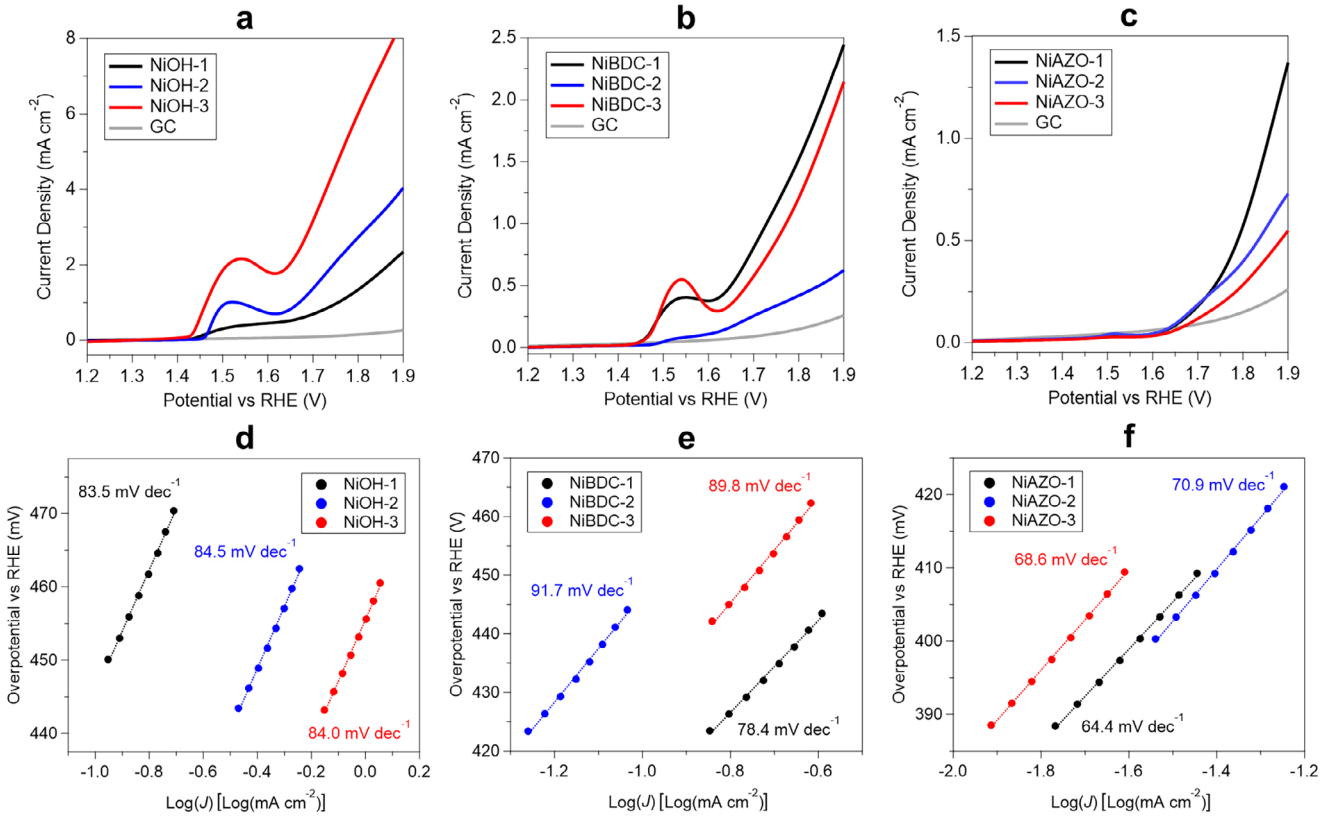

Figure 10. LSV curves of a) β-Ni(OH)$_2$, b) NiBDC, and c) NiAZO samples compared to that of bare GC electrode. Corresponding Tafel plots of d) β-Ni(OH)$_2$, e) NiBDC, and (f) NiAZO samples. Scan rate = 0.05 V s^{-1}, T = 25 °C, in 0.1 M aqueous KOH.

with the lowest E_{onset}. The similar slopes shown by all materials suggest that a similar electrocatalytic mechanism is involved, despite the observed differences in J_{CAT} (see Figure 11a–c). The activity of the catalysts studied in this work can be compared with the rich literature on similar MHOF, using the most common metrics, i.e., η_{CAT} of the OER reaction and Tafel slope, which are gathered in Table 6. We found that the performances of the NiL-*x* catalysts are in line with what already reported for Ni$_2$(OH)$_2$(BDC) and Ni$_2$(OH)$_2$(AZO).[7,21] It must be noted that a quantitative comparison of the catalytic activity with the literature is not straightforward, since the measurements depend on several factors, such as catalyst loading, nature of the working electrode, geometry of the electrochemical cell, scan rate, *i*R drop correction, use of a rotating electrode, etc.

The LSV curves in Figure 10 show that, even if the GC electrode was loaded with the same amount of material (0.035 mg cm^{-2}), the samples exhibit very different currents of the Ia signals due to a different number of Ni centers available for electron

Table 5. OER catalytic parameters of the β-Ni(OH)$_2$, NiBDC, and NiAZO samples, in 0.1 M aqueous KOH.

Catalyst	η_{CAT} (mV)[a]	$E_{OER,CAT}$ (V)[a]	E_{onset} (V)	Tafel Slope (mV dec^{-1})
NiOH-1	589	1.82	1.63	83.5
NiOH-2	494	1.72	1.62	84.5
NiOH-3	455	1.69	1.62	84.0
NiBDC-1	554	1.78	1.60	78.4
NiBDC-2	>670	>1.9	1.61	91.7
NiBDC-3	581	1.81	1.62	89.8
NiAZO-1	632	1.86	1.55	64.4
NiAZO-2	>670	>1.9	1.56	70.9
NiAZO-3	>670	>1.9	1.54	68.6

[a] At $J = 1$ mA cm^{-2}

transfer and catalysis. In fact, the intensity of Ia drops as the Ni content in the sample decreases (63%, 37%, and 28% in weight for β-Ni(OH)$_2$, NiBDC, and NiAZO, respectively). Instead, the differences within each family of materials are related to the different accessibility of the catalytic sites to the electrolyte, which can depend on factors such as morphology and size of the platelets. Therefore, we attempted to estimate the surface area of the samples measuring their BET areas by N_2 adsorption (Table 2). It is known that MHOFs possess lower surface areas (usually $<$ 100 m^2 g^{-1}) than conventional MOFs.[56] The BET surface areas of the NiBDC samples are in accordance with those already reported (from ~30 m^2 g^{-1} to ~100 m^2 g^{-1}).[7,57,58] However, in general, great care should be taken when comparing BET surface areas with literature data, since their values are strongly influenced by the degassing procedure and synthesis, which determine the size of the particles, their morphology, etc. The surface areas of NiAZO-2 and NiAZO-3 are similar and agree with the value reported by Yuan et al.[7] It is worth noting that the BET area of NiBDC-1 and NiAZO-1 are ~2 and ~2.5–3 times lower than those of their NiL-2 and NiL-3 analogues, respectively. This result can be probably ascribed to the fact that NiBDC-1 and NiAZO-1 contain residual NiOH-1, which possesses a very low BET area. Unfortunately, BET results do not correlate directly with the electrochemical trends. Finally, it must be considered that the proposed activation procedure could lead to sample dependent exfoliation and/or reconstruction phenomena.

In order to evaluate the catalytic efficiency of the Ni active sites in each sample, the catalytic LSV curves were normalized by the area of signal Ia, which is proportional to the number of available Ni sites. The normalized J_{CAT} values at +1.80 V allow to compare the catalytic efficiency of the single Ni centers, independently of their availability and accessibility, and regardless of the content of Ni^{2+} in the catalyst. The data reported in Figure 11d (and Figure S29) show that β-Ni(OH)$_2$, NiBDC-1, and NiBDC-3 have a rather similar normalized J_{CAT}, but NiBDC-2 behaves differently. It shows a lower J_{CAT} than NiBDC-1 and NiBDC-3 (Figure 11b), but its normalized J_{CAT} is by far the largest in the NiBDC family because the area of signal Ia in this particular sample is more than ten times lower than in NiBDC-1 and NiBDC-3. This is due to the fact that during the activation procedure the increase of signal Ia in NiBDC-2 is less pronounced (Figure S23), probably due to lower accessibility of the Ni sites. To explain this behavior a deep morphological study would be

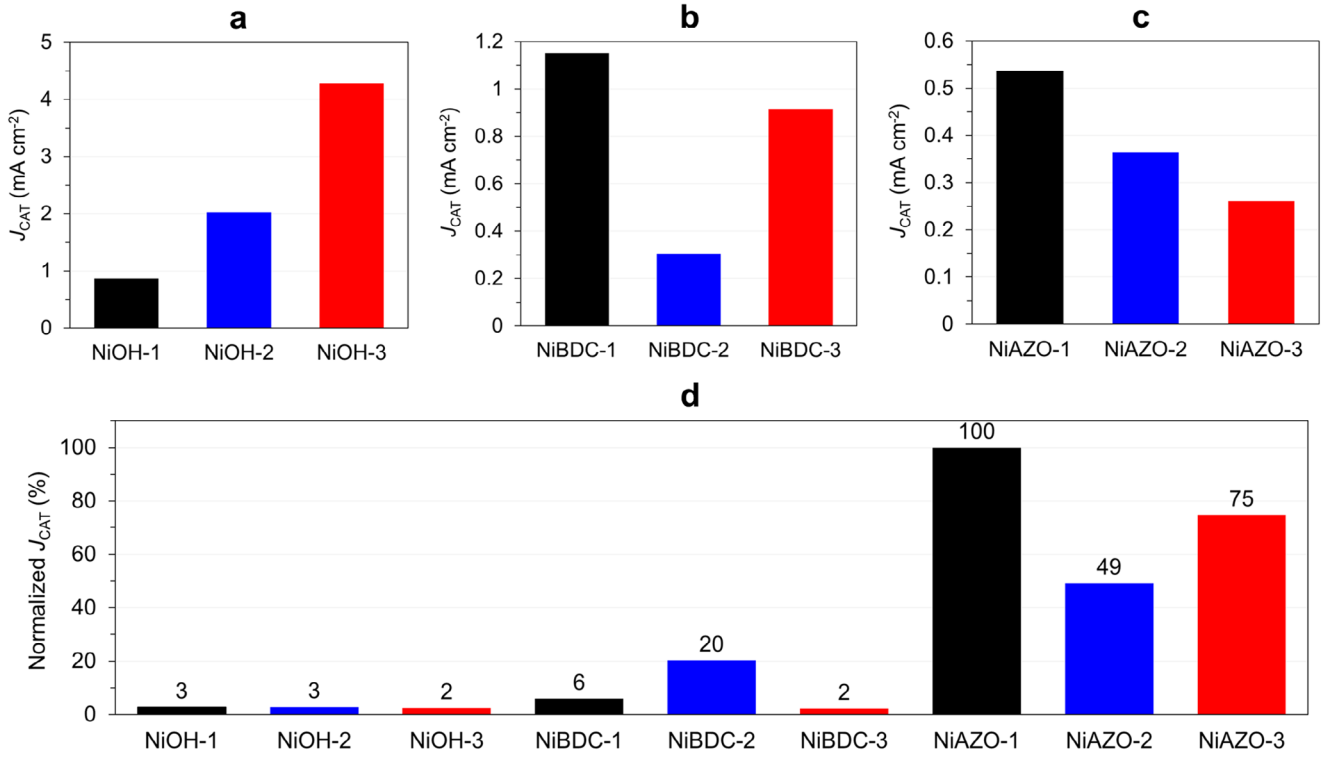

Figure 11. Panels a, b, and c: J_{CAT} at +1.80 V. Panel d: normalized J_{CAT} at +1.80 V (see Figure S29 for the ungrouped graphs).

Table 6. OER catalytic parameters of similar Ni MHOFs based on BDC^{2-} and AZO^{2-} linkers.

Catalyst	Electrolyte	η_{CAT} (mV)	Tafel Slope (mV dec^{-1})	Reference
$Ni_2(OH)_2(AZO)$	0.1 M KOH	530 (@1 mA cm^{-2})	61	[7]
$Ni_2(OH)_2(BDC)$	1 M KOH	404 (@10 mA cm^{-2})	74	[21]
NiFe-UMNs [L = BDC^{2-}]	1 M KOH	260 (@10 mA cm^{-2})	30	[54]
NiCo-UMOFNs [L = BDC^{2-}]	1 M KOH	250 (@10 mA cm^{-2})	42	[55]
HE-MHOF [L = BDC^{2-}]	1 M KOH	320 (@10 mA cm^{-2})	57	[14]

needed, which is, however, beyond the interest of this work. It is worth noting that J_{CAT} of β-$Ni(OH)_2$ samples increases as crystallinity increases (Figure 11a), while normalized J_{CAT} does not change (Figure 11d). Therefore, it can be concluded that the OER efficiency of β-$Ni(OH)_2$ mainly depends on the number of catalytic Ni active sites, whose availability and accessibility increase with crystallinity. Notably, the Ni sites in the NiAZO samples are exceedingly more active than those in β-$Ni(OH)_2$ and NiBDC (Figure 11d). This behavior agrees with the lower E_{onset} and Tafel slopes of the NiAZO samples, and with what reported in the literature.[7] Since the MHOF phases in NiBDC-*x* and NiAZO-*x* samples possess very similar crystallinity within each family, the differences in the catalytic activities of the samples are probably ascribable to residual unreacted NiOH-*x*. However, we cannot provide certain mechanistic insights on possible interactions between MHOF phases and residual NiOH-*x* phases.

To support the trends observed for J_{CAT}, the redox-derived turnover frequencies (TOF_{redox}) were also calculated, following the method proposed by Zheng et al. for NiBDC and NiAZO nanosheets.[15] The results are graphically shown in Figure S30 and agree with what described above. In particular, the TOF_{redox} values of NiAZO samples confirm that these are the catalysts of excellence in this study, since they are able to produce O_2 molecules around ten times faster than NiBDC and β-$Ni(OH)_2$ samples.

It is surprising that the highest value of normalized J_{CAT} is found in NiAZO-1, although this sample contains ~50% in weight of unreacted NiOH-1 (see Tables 2 and 3). NiAZO-1 being the most active catalyst in this work, its morphology was investigated by TEM, whose images are presented in Figure S14a–c. TEM analysis indicates that the NiAZO MHOF in NiAZO-1 (Figure S14a) possesses the same morphology found for NiAZO-3 (Figure S14d–f), in accordance with their similar crystallinity. The β-$Ni(OH)_2$ phase present in the same sample (Figure S14b,c) exhibits the same low crystalline morphology observed in the NiOH-1 precursor (Figure S1b,c), in accordance with QPA by Rietveld refinement. Surprisingly, the presence of NiOH-1 in NiAZO-1 is not evident from the electrochemical point of view, as the electrochemical properties of the Ni^{2+}/Ni^{3+} redox process (signals Ia and Ic) resemble those of NiAZO-2 and NiAZO-3 (see Figures 8 and S22). This means that the residual NiOH-1 in NiAZO-1 behaves differently from pure NiOH-1.

In an attempt to explain these unexpected findings, we prepared a new material (NiAZO-4) by admixing NiOH-1 and NiAZO-3 in ~1:1 ratio in weight to mimic the composition of NiAZO-1. The CV of NiAZO-4 (at ep1), presented in Figure S31, is significantly different from that of NiAZO-1. While the cathodic scan of NiAZO-1 is characterized by one signal (Ic), two different reduction peaks (Ic and IIc) are present for NiAZO-4 which can be assigned to the reduction of the NiAZO-3 and NiOH-1 fractions, respectively. This result confirms that the CV of NiAZO-1 does not match the sum of the electrochemical responses of NiAZO MHOF and unreacted NiOH-1. Unlike the cathodic curve, the anodic signal (Ia) of NiAZO-4 is not split, since the oxidations of NiAZO-3 and NiOH-1 are overlapped. The potential, shape, and intensity of Ia are however significantly different from those of NiAZO-1, confirming different electrochemical behaviors. NiAZO-1 and NiAZO-4 are otherwise almost identical from a compositional point of view, as shown by Rietveld refinement of their PXRD patterns (Figure S32 and Table S2). Therefore, a probable explanation is that the electrochemical response of unreacted NiOH-1 in NiAZO-1 is not visible as a consequence of surface transformation from β-$Ni(OH)_2$ to NiAZO phase (by surface intercalation of AZO^{2-}), which occurs during the synthesis of NiAZO-1 without altering the PXRD pattern of residual NiOH-1 (Figure S32). This is in accordance with what reported for Ni- or Ni/Fe-based hydroxides, which can be intercalated only superficially when exposed to carboxylate ligands.[20] The transformation leads to significant changes in the redox potential of the Ni species, as observed for NiAZO-1. Therefore, this NiAZO MHOF, supported on the surface of β-$Ni(OH)_2$ particles with very small crystallites, probably possesses an exceptional catalytic activity due to the high availability of its superficial Ni sites, which undergo reconstruction into more active NiOOH-like phases than those formed from pure β-$Ni(OH)_2$.[15,16] Moreover, the conductivity of the surface-modified β-$Ni(OH)_2$ particles is not lowered by the presence of the organic linker (which could hinder electron transfer during catalysis),[10] since the overall content of superficial AZO^{2-} is low. These effects may be interestinglyresponsible for the observed enhancement of the catalytic activity of NiAZO-1 compared to NiAZO-2 and NiAZO-3 (Figure 11).

3. Conclusions

For the first time, the crystallinity of the starting β-Ni(OH)$_2$ (low, intermediate, and high) was taken into account as a variable in the synthesis of two families of Ni^{2+}-based MHOFs, NiBDC, and NiAZO, which are well-known efficient catalysts for OER.[7] Interestingly, the degree of crystallinity of β-Ni(OH)$_2$ does not affect that of the synthesized MHOFs, which were found to be highly crystalline even starting from very low crystalline NiOH-1. On the other hand, unreacted β-Ni(OH)$_2$ preserved its initial crystallinity at the end of the solvothermal synthesis. These results demonstrate that the energy gained with the intercalation reaction of β-Ni(OH)$_2$ is the driving force for the effective removal of stacking faults disorder between the layers in β-Ni(OH)$_2$. In particular, this structural ordering by intercalation is efficient when BDC^{2-} is employed, while it is much less effective when NiOH-1 and H_2AZO are reacted together leading to NiAZO-1 sample, where residual NiOH-1 is found to be ~50% in weight. All the synthesized samples were deeply characterized in the solid state, aiming to reach a comprehensive description of structural and spectroscopic aspects which were not discussed in detail in the literature. In particular, combining FT-IR and UV–vis–NIR spectroscopies with the synthesis of a partially deuterated NiBDC sample (NiBDC*a*-d_2), we found that two inequivalent OH^- ions are present in ~1:1 ratio in the triclinic $P\bar{1}$ structure of NiBDC, where all the OH^- are reported to be equivalent.[7] Our results therefore indicate that this triclinic structure may require revision, a direction we are currently working in.

The electrocatalytic properties and stability of β-Ni(OH)$_2$ and MHOF samples for OER were studied in detail through CV measurements, in combination with diffuse reflectance UV–vis–NIR spectroscopy. We found that the catalytic efficiency of the single Ni active site in β-Ni(OH)$_2$ is crystallinity independent, while the number of available Ni sites increases with increasing crystallinity. The bulk of β-Ni(OH)$_2$ samples is very stable in the potential range of the Ni^{2+}/Ni^{3+} redox process (ep1, +1.56 V) while it undergoes significant reconstruction into NiOOH-like phases already at ep4 (+1.86 V). On the other hand, MHOF samples show much higher bulk electrochemical stability after CV cycling at ep4, indicating only a superficial transformation into the NiOOH-like active phase. Therefore, we proposed that CV cycling at progressively increasing endpoints from ep1 to ep4 can be a possible activation procedure for NiBDC and NiAZO MHOFs, which reconstruct into active NiOOH-like phases,[15,16] without affecting the stability of the bulk of the catalyst. After activation, the catalytic measurements can be performed through LSV at ep5 (+1.96 V), where no current drops due to significant structural reconstructions are observed for all the samples.

While the similarity between all Tafel plots points to a similar electrocatalytic mechanism for β-Ni(OH)$_2$ and MHOF samples, NiAZO samples exhibit the highest OER activity and electrochemical stability, in accordance with what already reported in the literature.[7] Surprisingly, NiAZO-1 was found to be the catalyst of excellence in this study, although it contains ~50% in weight of unreacted β-Ni(OH)$_2$ with low crystallinity (NiOH-1). We demonstrated that this residual NiOH-1 behaves differently from the corresponding pure phase during OER, its electrochemical response resembling that of a NiAZO-like catalyst. We propose that the superior catalytic activity of NiAZO-1 is probably ascribable to a superficial transformation from β-Ni(OH)$_2$ into the more efficient NiAZO phase, while the bulk material remains non-intercalated and maintains a good conductivity. This unexpected result paves the way for further studies on the synthesis, morphology, and catalytic activity of these appealing surface-like MHOFs supported on badly-crystalline β-Ni(OH)$_2$.

4. Experimental Section

4.1. General Methods

All reagents and solvents were used as received unless otherwise specified. Water was bi-distilled using a Milli-Q IQ 7000 system. *N*,*N*-dimethylformamide (DMF) was distilled under reduced pressure.[59] H_2AZO, NiBDC, and NiAZO MHOFs were synthesized modifying procedures reported in literature.[7] Elemental analysis was performed using a ThermoFisher Scientific Flash 2000 analyzer. FT-IR spectra were collected in ATR mode between 400 and 4000 cm^{-1} with a resolution of 2 cm^{-1}, using a JASCO 4700 FT-IR spectrometer. Solid-state UV–vis–NIR diffuse reflectance spectra were collected between 200 nm and 2500 nm, using a JASCO V-570 spectrometer (reported values are in absorbance = *A*). The following abbreviations are used to describe FT-IR and UV–vis–NIR data: vs, very strong; s, strong; m, medium; w, weak; br, broad; sh, shoulder. BET surface areas were measured by nitrogen adsorption, using a Micromeritics Chemisorb 2750. Prior to the measurement each sample was degassed at 110 °C for 1 h, under a H_2/N_2 flux. The NMR spectra were recorded at 298 K on an AVANCE400 FT-NMR spectrometer (600.13, 150.90, and 60.83 MHz for ^{1}H, ^{13}C, and ^{15}N, respectively) from Bruker Biospin. The spectra were processed using TopSpin (Version 4.3.0).[60] The chemical shifts (δ) are expressed in ppm downfield from tetramethylsilane (TMS) as external standard. The residual proton (carbon) signal of DMSO-d_6 was set to 2.50 ppm (39.52 ppm). The samples analyzed by TEM were suspended in EtOH and sonicated with ultrasounds for 5 min at room temperature. After this, a Cu microscope grid (200 mesh, carbon coated) was immersed in the suspension, then allowed to dry under IR radiation, and finally introduced inside a high-resolution scanning/transmission electron microscope (S/TEM) (Thermo Scientific, Waltham, MA, USA, Talos F200S) equipped with energy dispersive X-ray analysis (EDX).

4.2. Synthesis of Azobenzene-4,4′-dicarboxylic Acid (H_2AZO)

In a round bottom flask (500 mL), *p*-nitrobenzoic acid (15.003 g, 89.774 mmol) was dissolved in aqueous NaOH (225 mL, 5.5 M). The mixture was heated at 50 °C and a solution of glucose (100 g, 555 mmol in 150 mL of water) was added dropwise over 60 min. At the end, the red-brown mixture was air-bubbled for 2 h without stirring. A pink–orange solid was collected by filtration and dissolved in hot water, which was then acidified with glacial acetic acid until pH = 4 was reached. The precipitate was collected by filtration and then dried under vacuum at 75 °C, to give the product as an orange powder (6.400 g, 23.68 mmol, 52.8%).

Elemental analysis (%) calc. for H_2AZO (found): C = 62.22 (61.91), H = 3.73 (3.59), N = 10.37 (10.14). ^{1}H NMR (DMSO-d_6, 600.13 MHz, 298 K): δ_H = 13.3 (2H, br, COOH), 8.15 (4H, m, $H_{3,5}$), 8.00 (4H, m, $H_{2,6}$).

^{13}C NMR (DMSO-d_6, 150.90 MHz, 298 K): δ_C = 166.6 (COOH), 154.1 (C_1), 133.6 (C_4), 129.9 ($C_{3,5}$), 122.5 ($C_{2,6}$). ^{15}N NMR (DMSO-d_6, 60.83 MHz, 298 K): δ_N = 518 (trans N═N).[61]

4.3. Synthesis of β-Ni(OH)$_2$

4.3.1. NiOH-1

$NiSO_4{\cdot}6H_2O$ (3.0271 g, 11.516 mmol) was dissolved in water (5 mL) to give a clear green solution, which was then introduced in a flask containing a ~1 M NaOH aqueous solution (50 mL, 50 mmol). The light green suspension obtained was kept under stirring for 15 min and then centrifugated to collect a green solid. The solid was washed with water (6 × 25 mL) until neutral washings and then dried in vacuum at 70 °C for 24 h, to give the product (NiOH-1) as a fine green powder (773.0 mg, 8.338 mmol, yield = 72.4%).

Elemental analysis (%) calc. for $Ni(OH)_{1.92}(CO_3^{2-})_{0.03}(SO_4^{2-})_{0.01}{\cdot}0.4H_2O$ (found): C = 0.36 (0.36), H = 2.71 (2.75), S = 0.32 (0.31). FT-IR (ATR): $\tilde{\nu}_{max}$ (cm^{-1}) = 3640 (w), ~3300 (w, br), 1634 (w), ~1450 (w), 1360 (w), 1110 (w), ~610 (m, sh), ~510 (s). UV–vis–NIR (diffuse reflectance): λ_{max} (*A*) = 253 (0.40), 397 (0.44), 422 (sh), 678 (0.43), 740 (sh), ~1150 (br, 0.41), 1415 (0.36), 1939 (0.32), 2210 (0.29), 2340 (0.35), 2480 nm (0.49).

4.3.2. NiOH-2

$NiSO_4{\cdot}6H_2O$ (1.3170 g, 5.0105 mmol) was dissolved in water (5 mL) to give a clear green solution, which was then introduced in a Teflon liner (100 mL) containing a ~1 M NaOH aqueous solution (20 mL, 20 mmol), obtaining a light green suspension. The Teflon liner was put in a stainless-steel autoclave and was heated at 120 °C for 24 h. After cooling to room temperature, the suspension was centrifugated to collect a green solid. The workup followed the same steps reported for NiOH-1 and gave the product as a fine green powder (355.0 mg, 3.829 mmol, yield = 76.4%).

Elemental analysis (%) calc. for $Ni(OH)_{1.9}(CO_3^{2-})_{0.05}{\cdot}0.1H_2O$ (found): C = 0.63 (0.97), H = 2.21 (2.15). IR (ATR): $\tilde{\nu}_{max}$ (cm^{-1}) = 3634 (s), 1584 (w), ~1360 (w), 505 (s). UV–vis–NIR (diffuse reflectance): λ_{max} (*A*) = 245 (0.34), 293 (0.19), 390 (0.35), 420 (sh), 673 (0.36), 732 (sh), 1135 (br, 0.37), 1186 (0.36), 1423 (0.25), 1935 (0.17), 2016 (0.17), 2220 (0.27), 2340 (0.27), 2477 nm (0.60).

4.3.3. NiOH-3

The synthesis and the work-up were carried out similarly as described for NiOH-2 ($NiSO_4{\cdot};6H_2O$: 3.0815 g, 11.723 mmol; ~1 M aqueous NaOH: 47 mL, 47 mmol), but heating the mixture at 180 °C for 24 h. After work-up, the isolated product is a fine green powder (1.0416 g, 11.235 mmol, yield = 95.8%).

Elemental analysis (%) calc. for $Ni(OH)_2$ (found): C = 0.00 (0.13), H = 2.17 (2.13). IR (ATR): $\tilde{\nu}_{max}$ (cm^{-1}) = 3629 (s), ~500 (s). UV–vis–NIR (diffuse reflectance): λ_{max} (*A*) = 235 (0.36), 290 (0.06), 390 (0.37), 420 (0.35), 674 (0.48), 733 (0.46), 1137 (br, 0.58), 1186 (0.57), 1424 (0.42), 1930 (0.32), 2028 (0.34), 2220 (0.47), 2340 (0.59), 2477 nm (0.95).

4.4. Synthesis of [$Ni_2(OH)_2(BDC)$] (NiBDC)

4.4.1. NiBDC-1

A Pyrex test tube (20 mL) equipped with a magnetic stirrer was loaded with NiOH-1 (52.5 mg, 0.566 mmol), H_2BDC (54.8 mg, 0.330 mmol), DMF (8 mL), ethanol (0.5 mL), and water (0.5 mL). The green suspension was heated at 130 °C for 3 days. After cooling to room temperature, the mixture was centrifugated, washed with DMF (3 × 3 mL), washed with ethanol (3 × 3 mL), and then dried at 70 °C under vacuum, to give the product as a fine green powder (52.8 mg).

Elemental analysis (%) calc. for $Ni_2(OH)_2(BDC){\cdot}0.5Ni(OH)_2{\cdot}0.5H_2O$ (found): C = 25.91 (26.01), H = 2.17 (2.41), N = 0.00 (0.37). IR (ATR): $\tilde{\nu}_{max}$ (cm^{-1}) = 3610 (w), 3592 (w), 3527 (w), ~3300–3200 (w, br), 1580 (s), 1498 (w), 1428 (w), 1352 (s), 1310 (w), 1146 (w), 1099 (w), 1016 (w), 907 (w), 875 (w), 827 (sh), 813 (s), 747 (m), 688 (m), ~555 (m), ~520 (m), ~490 (m). UV–vis–NIR (diffuse reflectance): λ_{max} (*A*) = 270 (0.54), 294 (0.57), 329 (0.60), ~450 (sh), 683 (0.28), 745 (0.27), 1200 (br, 0.30), 1383 (0.28), 1417 (0.29), 1452 (sh), 1661 (0.23), 1932 (0.22), 2140 (sh), 2210 (sh), 2272 (0.38), 2327 (0.34), 2457 nm (0.36).

4.4.2. NiBDC-2

The synthesis was carried out similarly as described for NiBDC-1 (H_2BDC: 53.5 mg, 0.322 mmol), using NiOH-2 (51.3 mg, 0.553 mmol) as a source of nickel(II), to give the product as a fine green powder (72.2 mg).

Elemental analysis (%) calc. for $Ni_2(OH)_2(BDC){\cdot}0.4Ni(OH)_2$ (found): C = 27.25 (26.99), H = 1.94 (2.18), N = 0.00 (0.17). IR (ATR): $\tilde{\nu}_{max}$ (cm^{-1}) = 3610 (w), 3592 (w), 3526 (w), ~3300–3200 (w, br), 1576 (s), 1498 (w), 1427 (w), 1349 (s), 1311 (sh), 1145 (w), 1098 (w), 1016 (w), 906 (w), 890 (w), 826 (sh), 811 (s), 744 (m), 685 (m), ~555 (m), ~520 (m), ~480 (m). UV–vis–NIR (diffuse reflectance): λ_{max} (*A*) = 264 (sh), 298 (sh), 346 (0.69), ~455 (sh), 680 (0.41), 747 (0.39), 1165 (br, 0.38), 1383 (0.32), 1419 (0.34), 1452 (0.30), 1664 (0.24), 1929 (0.22), 2044 (sh), 2143 (0.20), 2273 (0.38), 2327 (0.33), 2374 (0.28), 2460 nm (0.36).

4.4.3. NiBDC-3

The synthesis was carried out similarly as described for NiBDC-1 (H_2BDC: 53.0 mg, 0.319 mmol), using NiOH-3 (51.1 mg, 0.551 mmol) as a source of nickel(II), to give the product as a fine green powder (63.5 mg, 73.1%).

Elemental analysis (%) calc. for $Ni_2(OH)_2(BDC)$ (found): C = 30.45 (30.42), H = 1.92 (2.20), N = 0.00 (0.20).

IR (ATR): $\tilde{\nu}_{max}$ (cm^{-1}) = 3610 (w), 3592 (w), 3527 (w), ~3300–3200 (w, br), 1579 (vs), 1498 (w), 1427 (w), 1351 (vs), 1310 (sh), 1146 (w), 1100 (w), 1016 (w), 904 (w), 876 (w), 825 (sh), 811 (vs), 748 (s), 685 (m), ~555 (m), ~520 (m), ~485 (m). UV–vis–NIR (diffuse reflectance): λ_{max} (*A*) = 164 (0.55), 294 (0.59), 331 (0.61), ~460 (sh), 684 (0.23), 747 (0.22), 1206 (br, 0.24), 1384 (0.23), 1419 (0.24), 1452 (0.21), 1664 (0.19), 1925 (0.16), ~2000 (sh), 2150 (sh), 2274 (0.34), 2327 (0.26), 2376 (0.22), 2411 (0.22), 2452 nm (0.28)

4.4.4. NiBDCa

The synthesis was carried out similarly as described for NiBDC-1 (H_2BDC: 203.5 mg, 1.225 mmol), using $NiCl_2{\cdot}6H_2O$ (204.2 mg, 0.8591 mmol) as a source of nickel(II) and the following solvent mixture: 16 mL DMF, 1 mL H_2O, and 1 mL EtOH. The isolated product is a fine green powder (29.7 mg, 21.9%).

Elemental analysis (%) calc. for $Ni_2(OH)_2(BDC)$ (found): C = 30.45 (30.85), H = 1.92 (2.28), N = 0.00 (0.45). IR (ATR): $\tilde{\nu}_{max}$ (cm^{-1}) = 3610 (w), 3594 (w), 3525 (w), ~3300–3200 (w, br), 1579 (versus), 1502 (w), 1427 (w), 1356 (vs), 1310 (sh), 1150 (w), 1092 (w), 1024 (w), 1016 (w), 904 (w), 875 (w), ~830 (sh), 817 (vs), 740 (s), 684 (m), 550 (m). UV–vis–NIR (diffuse reflectance): λ_{max} (*A*) = 292 (0.59), 678 (0.19), 746 (sh), 1104 (br, 0.15), 1420 (0.09), 1452 (0.07), 1664 (0.04), ~1950 (br, 0.04), 2276 (0.18), 2318 (0.17), 2352 nm (0.15).

4.4.5. NiBDCa-d_2

The synthesis was carried out similarly as described for NiBDC*a*, but employing D_2O instead of H_2O. Moreover, EtOH was not added to avoid H/D exchange.

Elemental analysis (%) calc. for $Ni_2(OD)_2(BDC)$ (found): C = 30.26 (29.65), H = 1.27 (2.29), D = 1.27 (not measured), N = 0.00 (0.30). IR (ATR): $\tilde{\nu}_{max}$ (cm^{-1}) = 3592 (w), 3526 (w), ~3300–3200 (w, br), 2663 (w), 2650 (w), 2603 (w), 1635 (w), 1577 (vs), 1503 (w), 1427 (w), 1360 (vs), 1310 (sh), 1150 (w), 1092 (w), 1024 (w), 1016 (sh), 926 (w), 875 (w), 831 (m), 812 (m), 740 (s), 648 (s), 610 (s), 544 (s). UV–vis–NIR (diffuse reflectance): λ_{max} (*A*) = 290 (0.66), 390 (sh), 434 (sh), 676 (0.21), 746 (sh), ~1100 (br, 0.15), 1664 (0.04), 1920 (0.04), 1954 (0.05), ~1990 (br, 0.03), ~2270 (0.13), ~2450 nm (0.15).

4.5. Synthesis of $[Ni_2(OH)_2(AZO)]$ (NiAZO)

4.5.1. NiAZO-1

A Pyrex test tube (20 mL) equipped with a magnetic stirrer was loaded with NiOH-1 (51.0 mg, 0.550 mmol), H_2AZO (83.7 mg, 0.310 mmol), DMF (16 mL), ethanol (1 mL), and water (1 mL). The orange suspension was heated at 130 °C for 3 days. After cooling to room temperature, the mixture was centrifugated, washed with DMF (3 × 3 mL), washed with ethanol (3 × 3 mL), and then dried at 70 °C under vacuum, to give the product as a fine orange powder (48.8 mg).

Elemental analysis (%) calc. for $Ni_2(OH)_2(AZO)\cdot 4.5Ni(OH)_2\cdot H_2O$ C = 19.67 (19.67), H = 2.48 (2.61), N = 3.28 (3.25). IR (ATR): $\tilde{\nu}_{max}$ (cm^{-1}) = 3613 (w), ~3300–3200 (w, br), 1657 (w), 1598 (m), 1562 (m), 1491 (w), 1408 (sh), 1368 (s), 1312 (w), 1221 (w), 1161 (w), 1137 (w), 1097 (w), 1009 (w), 869 (w), 859 (w), 820 (s), 793 (s), 707 (m), 683 (m), 635 (m), ~490 (m). UV–vis–NIR (diffuse reflectance): λ_{max} (*A*) = 294 (0.49), 403 (0.63), 489 (sh), 680 (0.14), 744 (sh), 1185 (br, 0.14), 1384 (0.11), 1417 (0.12), 1667 (0.05), 1931 (0.06), 2144 (0.04), 2206 (sh), 2274 (0.14), 2333 (0.11), 2463 nm (0.19).

4.5.2. NiAZO-2

The synthesis was carried out similarly as described for NiAZO-1 (H_2AZO: 85.6 mg, 0.317 mmol), using NiOH-2 (52.5 mg, 0.566 mmol) as a source of nickel(II), to give the product as a fine orange powder (74.3 mg).

Elemental analysis (%) calc. for $Ni_2(OH)_2(AZO)\cdot 0.2Ni(OH)_2$ (found): C = 38.38 (38.52), H = 2.39 (2.67), N = 6.39 (6.23). IR (ATR): $\tilde{\nu}_{max}$ (cm^{-1}) = 3613 (w), ~3300–3200 (w, br), 1660 (w), 1598 (m), 1562 (m), 1490 (w), 1408 (sh), 1368 (s), 1312 (w), 1222 (w), 1161 (w), 1139 (w), 1097 (w), 1009 (w), 869 (w), 859 (w), 820 (s), 790 (s), 703 (m), 680 (m), 635 (m), ~490 (m). UV–vis–NIR (diffuse reflectance): λ_{max} (*A*) = 294 (0.55), 404 (0.72), 490 (sh), 680 (0.14), 742 (sh), 1180 (br, 0.13), 1383 (0.10), 1417 (0.12), 1666 (0.07), 1919 (0.05), ~2000 (sh), 2143 (0.07), 2208 (0.10), 2272 (0.18), 2330 (sh), ~2400 (0.11), 2462 nm (0.19).

4.5.3. NiAZO-3

The synthesis was carried out similarly as described for NiAZO-1 (H_2AZO: 84.3 mg, 0.312 mmol), using NiOH-2 (51.7 mg, 0.558 mmol) as a source of nickel(II), to give the product as a fine orange powder (93.5 mg).

Elemental analysis (%) calc. for $Ni_2(OH)_2(AZO)\cdot 0.15Ni(OH)_2$ (found): C = 38.79 (38.64), H = 2.39 (2.80), N = 6.46 (6.29). IR (ATR): $\tilde{\nu}_{max}$ (cm^{-1}) = 3613 (w), ~3300–3200 (w, br), 1660 (w), 1598 (m), 1562 (m), 1490 (w), 1408 (sh), 1368 (s), 1312 (w), 1221 (w), 1162 (w), 1139 (w), 1098 (w), 1009 (w), 869 (w), 859 (w), 820 (s), 792 (s), 706 (m), 681 (m), 636 (m), ~490 (m). UV–vis–NIR (diffuse reflectance): λ_{max} (*A*) = 299 (0.59), 403 (0.75), 490 (sh), 680 (0.12), 742 (sh), 1180 (br, 0.10), 1382 (0.07), 1416 (0.09), 1667 (0.06), 1920 (0.04), ~2000 (sh), 2144 (0.05), 2204 (0.06), 2273 (0.15), ~2395 (br, 0.08), 2462 nm (0.15).

4.6. X-ray Diffraction

Powder X-ray diffraction (PXRD) was carried out at room temperature (293 K) with a Malvern-Panalytical Empirean MultiCore X-ray powder diffractometer, equipped with an Empirean tube Cu LFF HR (High Resolution) (wavelength, λ = 1.54056 Å) at 40 kV and 40 mA. The intensities of the PXRD patterns plotted in each Figure of this work (and in the ESI) were only normalized in "counts per seconds".

The calculation of the average crystallite size through Scherrer formula and W-H method was performed using the specific tools implemented in the Xpert HighScore software (Version 3.0.5).[62] The Rietveld method for domain size analysis and QPA was performed using the commercial GSAS-II software (Version 4571).[63] In the three methods, instrumental broadening was taken into account, and it was determined using LaB_6 Standard Reference Material (NIST SRM660a, size of crystallites = 2.0 μm). The GSAS refinement was carried out according to the following features: i) the background was fitted with a Chebyshev function with a different number of coefficients depending on its complexity (21 for NiOH-1, 18 for NiOH-2, and 9 for NiOH-3); ii) the broadening of the peaks was modeled using the uniaxial domain size model implemented in the software, along the (00*l*) directions; iii) lattice parameters, scaling, phase fraction, and the coefficient corresponding to sample displacement were also refined.

Regarding the QPA of NiBDC samples, both triclinic ($P\bar{1}$) and monoclinic ($C2/m$) phases of NiBDC (CCDC 2120871 and CCDC 985792, respectively) along with β-$Ni(OH)_2$ (CCDC 1600072) were used as starting structural models. For the NiAZO samples only the triclinic ($P\bar{1}$) phase (CCDC 2120870) and the β-$Ni(OH)_2$ precursor were considered. The adopted refinement strategy was similar to the one described above to model the β-$Ni(OH)_2$ samples. For each sample, the average crystallite size of the β-$Ni(OH)_2$ precursor was fixed during refinement, to demonstrate that its crystallinity does not change during the synthesis of the corresponding MHOF (since all the Rietveld fits were possible in these conditions).

4.7. XANES Measurements

O K- and Ni $L_{3,2}$-edges XANES spectra were collected at the BACH beamline of IOM-CNR (ELETTRA, Trieste, Italy)[64] during experiment 20225170. Ex-situ powder samples and reference compounds were deposited on Ta. Sample holder was then loaded in ultra-high vacuum and the spectra were collected both in TEY mode (using a pico-ammeter Keithley 428 current amplifier connected to the sample holder to measure the drain current) and TFY mode (using an MCP Hamamatsu F4655-13). SG3 grating of the Variable Angle Spherical Grating (VASG) monochromator was used, with an energy resolution of 0.25 eV. The photon energy was calibrated measuring Au 4f XPS spectra of the Au foil with photon excitation in the first and second order of diffraction. For spectra collected at O K-edge, the commonly used normalization of the absorptance step equal to 1 has been performed using the Athena software,[65] whereas spectra collected at Ni L-edges were treated with IgorPro software (Version 8.04) for the background subtraction and normalization (in this case, intensities were normalized according to the more intense peak of the Ni L_3-edge around 854 eV). All spectra were collected

with a fixed energy step, equal to 0.25 eV. The alignment of the energy scale of XANES data collected at the O K-edge has been done according to the first peak of NiO reported.[47,66–68] It is however worth to highlight that in another paper, a different energy calibration for O K-edge data has been chosen[69] (−1.8 eV with respect to our choice). NiO was used as energy reference because of the abundance of reported O K-edge XANES spectra for this material. By contrast, to the best of our knowledge, the available data on $Ni(OH)_2$ are limited to those reported in Ref. [70] (energy shifted of −2 eV), Ref. [48] (energy shifted of +0.6 eV), and very recently in Ref. [50].

4.8. Electrochemistry

Electrochemical measurements were performed with an Autolab Potentiostat (Metrohom) mod. Vionic combined with INTELLO management program. A small volume glass cell was used, thermostated at 298 K. A GC electrode (surface area 0.071 cm^2), a $Ag/AgCl/KCl_{sat}$ electrode, and a Pt wire were used as working, reference, and counter electrode, respectively. The GC electrode was polished with an alumina slurry (Sigma Aldrich) and washed in an ultrasonic bath for about five minutes prior to use. Surface coating was then performed by drop casting with 1 µL of ink prepared by mixing 1 mg of the Ni sample, 400 µL of a water/isopropanol solution (2:1 v/v), and 12 µL of Nafion perfluorinated resin solution (5% m/m, D521CS Ion Power). Eventually, the surface was heated in an oven at 70 °C for 30 min to evaporate the solvents. The loading content of the Ni sample on the GC electrode was about 0.035 mg/cm^2. All the electrochemical measurements were carried out in 0.1 M aqueous KOH. All the reported potentials are referred to the RHE and were calculated using the following Equation (1):

$$E_{RHE} = E_{Measured} + E^0{}_{Ag/AgCl} + 0.059pH \quad (1)$$

The LSV curved were corrected for the *i*R drop, by subtracting the ohmic drop to the measured potential using Equation (2):

$$E_{corrected} = E_{experimental} - iR \quad (2)$$

where *i* is the measured current and *R* is the electrolyte resistance determined by the impedance of high-frequency alternating current at a nonfaradic potential.

To evaluate the catalytic parameters and currents, we separated the contribution of the Ni^{2+}/Ni^{3+} oxidation process (Ia) from that of OER. To do so, we subtracted from the experimental data the current density of the local minimum before the OER catalysis (IIa), as shown in Figure S28.

Acknowledgments

This project has been funded under: the National Recovery and Resilience Plan (NRRP), Mission 4 Component 2, Investment 1.5 – NextGenerationEU, Call for tender n. 3277 dated 30/12/2021, Award Number: 0001052 dated 23/06/2022; Progetto P20227P7WZ – CUP E53D23015850001 – NRRP Mission 4 Component 2, Investment 1.1 – NextGenerationEU e PRIN – NextGenerationEU – rif. D.D. N. 1409 MUR 14/09/2022. S.N and E.M. received support from the Italian government (Ministero dell'ambiente e della sicurezza energetica – Progetto PERMANENT – BANDO MITE PNRR Missione 2 Investimento 3.5 A – RSH2A-0O0012 and Ministero dell'Università e della Ricerca (MUR), funded by the European Union – NextGenerationEU – Project Title "NoblE metals free hierarchical Catalysts and eLectrocatalysts engIneering: in oPerando mulTi-technIque approaCh (ECLIPTIC)", ProjectNo. 2022A2A9NW-CUP: B53D2301357000, Mission 4, Component 2, Investment 1.1); Fondazione di Modena under the grant FAR Mission Oriented 2022 – FOMO line, CUP: E93C22000800007. The authors acknowledge Elettra Sincrotrone Trieste for providing access to its synchrotron radiation facilities and for financial support under the SUI internal project.

Open access publishing facilitated by Università degli Studi di Modena e Reggio Emilia, as part of the Wiley - CRUI-CARE agreement.

Conflict of Interests

The authors declare no conflict of interest.

Data Availability Statement

The data that support the findings of this study are available from the corresponding author upon reasonable request.

Keywords: Crystallinity · Electrochemical water splitting · Intercalation reaction · Metal hydroxide organic frameworks · Oxygen evolution reaction

[1] A. Raveendran, M. Chandran, R. Dhanusuraman, *RSC Adv.* **2023**, *13*, 3843–3876.
[2] Y. Yan, B. Y. Xia, B. Zhao, X. Wang, *J Mater. Chem. A* **2016**, *4*, 17587–17603.
[3] Y. Jiao, Y. Zheng, M. Jaroniec, S. Z. Qiao, *Chem. Soc. Rev.* **2015**, *44*, 2060–2086.
[4] N.-T. Suen, S.-F. Hung, Q. Quan, N. Zhang, Y.-J. Xu, H. M. Chen, *Chem. Soc. Rev.* **2017**, *46*, 337–365.
[5] F. Song, L. Bai, A. Moysiadou, S. Lee, C. Hu, L. Liardet, X. Hu, *J. Am. Chem. Soc.* **2018**, *140*, 7748–7759.
[6] S. Lee, Y.-C. Chu, L. Bai, H. M. Chen, X. Hu, *Chem. Catal.* **2023**, *3*, 100475.
[7] S. Yuan, J. Peng, B. Cai, Z. Huang, A. T. Garcia-Esparza, D. Sokaras, Y. Zhang, L. Giordano, K. Akkiraju, Y. G. Zhu, R. Hübner, X. Zou, Y. Román-Leshkov, Y. Shao-Horn, *Nat. Mater.* **2022**, *21*, 673–680.
[8] Y. Chen, P. Liao, K. Jin, Y. Zheng, H. Shao, G. Li, *Inorg. Chem. Front.* **2023**, *10*, 6489–6505.
[9] Y. Yan, T. He, B. Zhao, K. Qi, H. Liu, B. Y. Xia, *J. Mater. Chem. A* **2018**, *6*, 15905–15926.
[10] W. Zheng, L. Y. S. Lee, *ACS Energy. Lett.* **2021**, *6*, 2838–2843.
[11] R. Freund, O. Zaremba, G. Arnauts, R. Ameloot, G. Skorupskii, M. Dincă, A. Bavykina, J. Gascon, A. Ejsmont, J. Goscianska, M. Kalmutzki, U. Lächelt, E. Ploetz, C. S. Diercks, S. Wuttke, *Angew. Chem., Int. Ed.* **2021**, *60*, 23975–24001.
[12] B. D. McCarthy, A. M. Beiler, B. A. Johnson, T. Liseev, A. T. Castner, S. Ott, *Coord. Chem. Rev.* **2020**, *406*, 213137.
[13] W. Zheng, M. Liu, L. Y. S. Lee, *ACS Catal.* **2020**, *10*, 81–92.
[14] A. Roy, S. Kumar, A. Guilherme Buzanich, C. Prinz, E. Götz, A. Retzmann, T. Hickel, B. Bhattacharya, F. Emmerling, *Adv. Mater.* **2024**, *36*, 2408114.
[15] D. J. Zheng, M. Görlin, K. McCormack, J. Kim, J. Peng, H. Xu, X. Ma, J. M. LeBeau, R. A. Fischer, Y. Román-Leshkov, Y. Shao-Horn, *Chem. Mater.* **2023**, *35*, 5017–5031.
[16] X. Ma, D. J. Zheng, S. Hou, S. Mukherjee, R. Khare, G. Gao, Q. Ai, B. Garlyyev, W. Li, M. Koch, J. Mink, Y. Shao-Horn, J. Warnan, A. S. Bandarenka, R. A. Fischer, *ACS Catal.* **2023**, *13*, 7587–7596.
[17] H. Bode, K. Dehmelt, J. Witte, *Electrochim. Acta* **1966**, *11*, 1079–1087.

[18] S. Singha Roy, R. Madhu, A. Karmakar, S. Kundu, *ACS Mater. Lett.* **2024**, *6*, 3112–3123.
[19] Y. Chen, Q. Li, Y. Lin, J. Liu, J. Pan, J. Hu, X. Xu, *Nat. Commun.* **2024**, *15*, 7278.
[20] S. Hou, L. Xu, S. Mukherjee, J. Zhou, K.-T. Song, Z. Zhou, S. Zhang, X. Ma, J. Warnan, A. S. Bandarenka, R. A. Fischer, *ACS Catal.* **2024**, *14*, 12074–12081.
[21] X. Ma, L. Schröck, G. Gao, Q. Ai, M. Zarrabeitia, C. Liang, M. Z. Hussain, R. Khare, K.-T. Song, D. J. Zheng, M. Koch, I. E. L. Stephens, S. Hou, Y. Shao-Horn, J. Warnan, A. S. Bandarenka, R. A. Fischer, *ACS Catal.* **2024**, *14*, 15916–15926.
[22] J. Zhou, Y. Dou, X. Wu, A. Zhou, L. Shu, J. Li, *Small* **2020**, *16*, 1906564.
[23] D. S. Hall, D. J. Lockwood, C. Bock, B. R. MacDougall, *Proc. R. Soc. A.* **2015**, *471*, 20140792, h
[24] B. Shruthi, V. Bheema Raju, B. J. Madhu, *Spectrochim. Acta,Part A.* **2015**, *135*, 683–689.
[25] C. Liu, Y. Li, P. Li, C. Xing, *Mater. Res. Bull.* **2010**, *45*, 2001–2005.
[26] C. Delmas, C. Tessier, *J. Mater. Chem.* **1997**, *7*, 1439–1443.
[27] L. Dong, Y. Chu, W. Sun, *Chem. – Eur. J.* **2008**, *14*, 5064–5072.
[28] T. N. Ramesh, P. V. Kamath, *J. Power. Sources.* **2006**, *156*, 655–661.
[29] C. Faure, C. Delmas, M. Fouassier, *J. Power. Sources.* **1991**, *35*, 279–290.
[30] M. C. Bernard, P. Bernard, M. Keddam, S. Senyarich, H. Takenouti, *Electrochim. Acta.* **1996**, *41*, 91–93.
[31] G. J. de, A. A. Soler-Illia, M. Jobbágy, A. E. Regazzoni, M. A. Blesa, *Chem. Mater.* **1999**, *11*, 3140–3146.
[32] K. Lawson, S. P. Wallbridge, A. E. Catling, C. A. Kirk, S. E. Dann, *J. Mater. Chem. A* **2023**, *11*, 789–799.
[33] P. Scherrer, Nachrichten von der Gesellschaft der Wissenschaften zu Göttingen, Mathematisch-Physikalische Klasse, **1918**, *1918*, 98–100.
[34] S. Deabate, F. Fourgeot, F. Henn, *J. Power. Sources.* **2000**, *87*, 125–136.
[35] T. N. Ramesh, *Mater. Chem. Phys.* **2009**, *114*, 618–623.
[36] K. Nakamoto, *Infrared and Raman Spectra of Inorganic and Coordination Compounds*, John Wiley & Sons, Inc, New Jersey **2008**.
[37] A. Mesbah, P. Rabu, R. Sibille, S. Lebègue, T. Mazet, B. Malaman, M. François, *Inorg. Chem.* **2014**, *53*, 872–881.
[38] K. Hadjiivanov, *Advances in Catalysis* (Ed: F. C. Jentoft), Academic Press, Massachusetts, **2014**, *57*, pp. 99–318.
[39] G. Deacon, *Coord. Chem. Rev.* **1980**, *33*, 227–250.
[40] K. I. Hadjiivanov, D. A. Panayotov, M. Y. Mihaylov, E. Z. Ivanova, K. K. Chakarova, S. M. Andonova, N. L. Drenchev, *Chem. Rev.* **2021**, *121*, 1286–1424.
[41] E. L. Markun, D. A. Jensen, J. D. Vegetabile, J. A. Kaduk, *Acta. Crystallogr. E Crystallogr. Commun.* **2022**, *78*, 584–589.
[42] V. Zeleňák, Z. Vargová, K. Györyová, *Spectrochim Acta., Part A.* **2007**, *66*, 262–272.
[43] A. B. P. Lever, *Inorganic Electronic Spectroscopy*, Elsevier, Amsterdam, **1984**.
[44] K. Jayanthi, K. Fazl-Ur-Rahman, P. V. Kamath, G. Periyasamy, *Spectrochim. Acta., Part A.* **2020**, *233*, 118192.
[45] B. Weckler, H. D. Lutz, *Spectrochim. Acta., Part A* **1996**, *52*, 1507–1513.
[46] L. G. Weyer, S.-C. Lo, in *Handbook of Vibrational Spectroscopy* (Eds.: P. Griffiths, J. M. Chalmers), John Wiley & Sons, New Jersey **2006**.
[47] F. Frati, M. O. J. Y. Hunault, F. M. F. de Groot, *Chem. Rev.* **2020**, *120*, 4056–4110.
[48] X. Wang, S. Xi, W. S. V. Lee, P. Huang, P. Cui, L. Zhao, W. Hao, X. Zhao, Z. Wang, H. Wu, H. Wang, C. Diao, A. Borgna, Y. Du, Z. G. Yu, S. Pennycook, J. Xue, *Nat. Commun.* **2020**, *11*, 4647.
[49] S. Nappini, L. D'Amario, M. Favaro, S. Dal Zilio, F. Salvador, E. Betz-Güttner, A. Fondacaro, I. Píš, L. Romanzin, A. Gambitta, F. Bondino, M. Lazzarino, E. Magnano, *Rev. Sci. Instrum.* **2021**, *92*, 015115.
[50] H. Moreno Fernández, J. Gallenberger, C. Mempin, I. Khalek, M. Neumann, S. Lotfi, S. M. Kim, M. Li, C. Tian, J. P. Hofmann, *Electrochim. Acta.* **2024**, *498*, 144626.
[51] C. Kuai, Y. Zhang, D. Wu, D. Sokaras, L. Mu, S. Spence, D. Nordlund, F. Lin, X.-W. Du, *ACS Catal.* **2019**, *9*, 6027–6032.
[52] M. Al Samarai, A. W. Hahn, A. Beheshti Askari, Y.-T. Cui, K. Yamazoe, J. Miyawaki, Y. Harada, O. Rüdiger, S. DeBeer, *ACS Appl. Mater. Interfaces* **2019**, *11*, 38595–38605.
[53] H. A. El-Sayed, A. Weiß, L. F. Olbrich, G. P. Putro, H. A. Gasteiger, *J. Electrochem. Soc.* **2019**, *166*, F458–F464.
[54] G. Hai, X. Jia, K. Zhang, X. Liu, Z. Wu, G. Wang, *Nano Energy.* **2018**, *44*, 345–352.
[55] S. Zhao, Y. Wang, J. Dong, C.-T. He, H. Yin, P. An, K. Zhao, X. Zhang, C. Gao, L. Zhang, J. Lv, J. Wang, J. Zhang, A. M. Khattak, N. A. Khan, Z. Wei, J. Zhang, S. Liu, H. Zhao, Z. Tang, *Nat. Energy.* **2016**, *1*, 16184.
[56] M. J. Kalmutzki, N. Hanikel, O. M. Yaghi, *Sci. Adv.* **2018**, *4*, eaat9180.
[57] K. Song, S. Liang, X. Zhong, M. Wang, X. Mo, X. Lei, Z. Lin, *Appl. Catal. B* **2022**, *309*, 121232.
[58] N. K. Gupta, J. Bae, S. Kim, K. S. Kim, *RSC Adv.* **2021**, *11*, 8951–8962.
[59] W. L. F. Armarego, *Purification of Laboratory Chemicals*, Butterworth–Heinemann, Oxford, UK, **2017**.
[60] B. A. X. S. Inc., TopSpin 4.3.0, Bruker AXS Inc., Madison, WI, USA, **2023**.
[61] K. A. Thorn, *PLoS One* **2019**, *14*, e0224112.
[62] T. Degen, M. Sadki, E. Bron, U. König, G. Nénert, *Powder Diffr.* **2014**, *29*, S13–S18.
[63] B. H. Toby, R. B. Von Dreele, *J. Appl. Crystallogr.* **2013**, *46*, 544–549.
[64] M. Zangrando, M. Zacchigna, M. Finazzi, D. Cocco, R. Rochow, F. Parmigiani, *Rev. Sci. Instrum.* **2004**, *75*, 31–36.
[65] B. Ravel, M. Newville, *J. Synchrotron Radiat.* **2005**, *12*, 537–541.
[66] C. Mitterbauer, G. Kothleitner, W. Grogger, H. Zandbergen, B. Freitag, P. Tiemeijer, F. Hofer, *Ultramicroscopy* **2003**, *96*, 469–480.
[67] D. Drevon, M. Görlin, P. Chernev, L. Xi, H. Dau, K. M. Lange, *Sci. Rep.* **2019**, *9*, 1532.
[68] R. Li, S. Yang, Y. Zhang, G. Yu, C. Wang, C. Chen, G. Wu, R. Sun, G. Wang, X. Zheng, W. Yan, G. Wang, D. Rao, X. Hong, *Cell. Rep. Phys. Sci.* **2022**, *3*, 100788.
[69] H. Y. Peng, Y. F. Li, W. N. Lin, Y. Z. Wang, X. Y. Gao, T. Wu, *Sci. Rep.* **2012**, *2*, 442.
[70] J. Zhang, X. Wu, W.-C. Cheong, W. Chen, R. Lin, J. Li, L. Zheng, W. Yan, L. Gu, C. Chen, Q. Peng, D. Wang, Y. Li, *Nat. Commun.* **2018**, *9*, 1002.

Manuscript received: May 30, 2025
Revised manuscript received: July 10, 2025
Accepted manuscript online: July 13, 2025
Version of record online: ■■, ■■